

---

# HYPERGRAPH GENERATION VIA STRUCTURED STOCHASTIC DIFFUSION

---

**Christopher Nemeth**  
 School of Mathematical Sciences  
 Lancaster University  
 c.nemeth@lancaster.ac.uk

May 7, 2026

## ABSTRACT

Hypergraphs model higher-order interactions, but realistic hypergraph generation remains difficult because incidence, hyperedge-size heterogeneity, and overlap structure are not faithfully captured by pairwise reductions. We propose HEDGE, a generative model defined directly on relaxed incidence matrices via a structured stochastic diffusion. The forward process combines a hypergraph-specific two-sided heat operator with an Ornstein–Uhlenbeck component, preserving structure-aware noising near the data while yielding an explicit Gaussian terminal law. Conditional on an observed hypergraph, this forward process is linear-Gaussian, so conditional means, covariances, scores, and reverse-drift targets are available in closed form. We therefore learn a permutation-equivariant state-only reverse-drift field in incidence space by regressing onto exact conditional targets, and generate samples by simulating a learned reverse-time SDE from the Gaussian base law. We establish exactness in the ideal state-only setting together with finite-horizon stability guarantees, and empirically show improved hypergraph generation quality relative to strong baselines.

## 1 Introduction

Hypergraphs extend ordinary graphs by allowing a single relation to involve any number of nodes [3]. This makes them a natural model for systems whose interactions are inherently group-based rather than pairwise, such as coauthorship networks [32], group-based communication and social interaction [4], item co-purchase data [41], and biological interaction systems [24]. In such settings, the object of interest is not merely whether two nodes are connected, but which subsets of nodes participate together in a shared interaction. This structure is represented explicitly through the *node-hyperedge incidence matrix*; Figure 1 gives a simple actor–movie example.

This additional expressivity makes hypergraph generation substantially more challenging. A graph generator models pairwise adjacency [42; 39; 46; 31], whereas a hypergraph generator must capture node participation across hyperedges, the distribution of hyperedge sizes, and the overlap structure induced by shared node memberships. These features encode the higher-order organisation of the system and are often distorted or lost under pairwise reductions such as clique expansions [1; 47]. Consequently, realistic hypergraph generation requires models that operate in a representation where these structural properties are native rather than reconstructed post-hoc.

Our starting point is that hypergraph incidence matrices admit a natural two-sided smoothing mechanism: one operator acts across nodes with similar hyperedge participation patterns, and another acts across overlapping hyperedges. Together, these define a hypergraph-aware heat flow on relaxed incidence matrices, giving an inductive bias that is intrinsic to the observed hypergraph. However, pure heat flow contracts towards a hypergraph-dependent low-complexity endpoint rather than a universal non-degenerate base law. To overcome this, we introduce Hyper Edge Diffusion and GEneration (HEDGE), a *structured stochastic diffusion* in incidence space that follows the two-sided heat operator near the data and gradually transitions to an Ornstein–Uhlenbeck (OU) regime at later times. This *heat–OU process* preserves structure-aware noising while yielding an explicit Gaussian terminal law. We show that the forward process is linear-Gaussian conditional on the observed hypergraph, so its conditional means, covariances, and reverse-drift

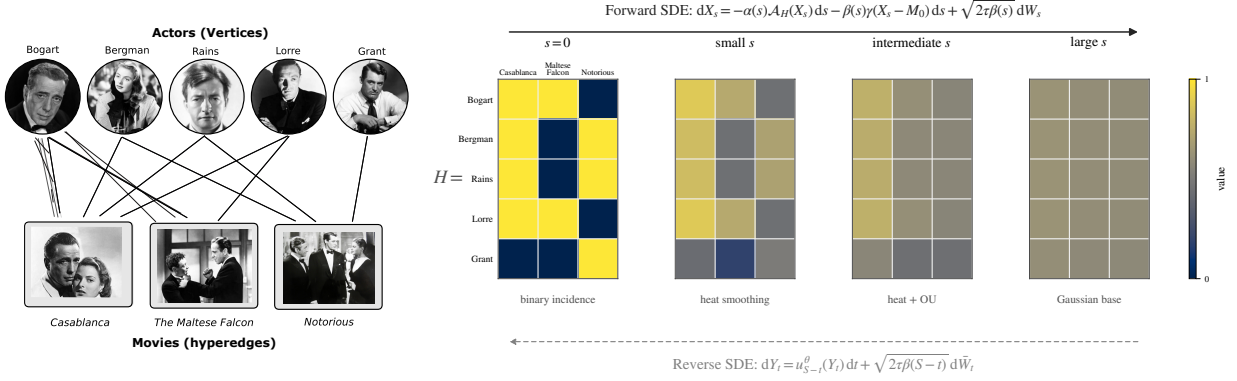


Figure 1: Left: An actor–movie hypergraph. Right:  $H$  is the incidence matrix representation of the hypergraph, where rows correspond to actors, columns to movies, and  $H_{ij} = 1$  indicates that actor  $i$  appears in movie  $j$ . The forward SDE removes the hypergraph structure and converges to a Gaussian terminal distribution. The reverse SDE reconstructs the hypergraph from Gaussian initialisation.

targets are all computable. We therefore learn an  $S_n \times S_m$ -equivariant reverse-drift model directly on relaxed incidence matrices and generate samples by integrating a learned reverse-time SDE.

**Our contributions.** (i) We introduce HEDGE, a structured stochastic diffusion for hypergraph generation in incidence space that combines hypergraph-specific two-sided heat smoothing with an Ornstein–Uhlenbeck regime, yielding an explicit Gaussian terminal law. (ii) We formulate reverse-time learning as regression onto exact conditional reverse-drift targets, and show that the  $L^2$ -optimal state-only predictor is the posterior average of these conditional reverse drifts; when the marginal reverse dynamics admit a state-only representation, this coincides with the marginal reverse drift. (iii) We prove finite-horizon stability guarantees for reverse generation in Wasserstein distance, clarifying how generation error depends on reverse-drift approximation and numerical discretisation. (iv) We identify the natural  $S_n \times S_m$  symmetry class of the reverse process, and show that the  $L^2$ -optimal state-only target is itself equivariant, motivating an  $S_n \times S_m$ -equivariant neural parameterisation. (v) We empirically show improved hypergraph generation quality over strong statistical baselines on real-data benchmarks.

## 2 Preliminaries

**Hypergraphs and incidence matrices.** A hypergraph is represented by the pair  $\mathcal{H} = (V, E)$ , where  $V = \{1, \dots, n\}$  is a finite node set and  $E = \{e_1, \dots, e_m\}$  is a multiset of non-empty hyperedges with  $e_j \subseteq V$ . Throughout, we consider unweighted undirected hypergraphs and assume no isolated nodes and no empty hyperedges. The incidence matrix of  $\mathcal{H}$  is the binary matrix

$$H \in \{0, 1\}^{n \times m}, \quad H_{v,e} = 1 \iff v \in e.$$

Rows of  $H$  record node participation across hyperedges, while columns record the members of each hyperedge. Two basic marginals derived from  $H$  are the node-degree and hyperedge-size vectors,

$$d_V := H\mathbf{1}_m \in \mathbb{N}^n, \quad d_E := H^\top \mathbf{1}_n \in \mathbb{N}^m, \quad (1)$$

where  $d_V(v)$  is the number of hyperedges incident to node  $v$ , and  $d_E(e)$  is the size of hyperedge  $e$ . We embed binary incidence matrices in a continuous state space by considering relaxed incidence states  $X \in \mathbb{R}^{n \times m}$ . This lets us define stochastic processes and differential operators directly in incidence space, which will allow for continuous-space reverse-time hypergraph generation.

**Node-side and hyperedge-side operators.** We view  $X \in \mathbb{R}^{n \times m}$  as an element of a Euclidean space equipped with the Frobenius inner product  $\langle X, Y \rangle_F := \text{tr}(X^\top Y)$ . The incidence matrix has two natural domains: rows indexed by nodes and columns indexed by hyperedges. Since our model evolves relaxed incidence matrices directly, we introduce one operator on each side. On the node side, we use the normalised hypergraph Laplacian of Zhou et al. [47]; Chan et al. [9],

$$L_V(H) = I_n - D_V^{-1/2} H D_E^{-1} H^\top D_V^{-1/2}, \quad D_V := \text{diag}(d_V), \quad D_E := \text{diag}(d_E). \quad (2)$$

This operator *smooths node-level signals* across nodes with similar hyperedge patterns. Whenever inverse degree matrices appear, inversion is understood entrywise on strictly positive diagonal entries, with zero assigned to zero

diagonal entries. Under the no-isolated-node and no-empty-hyperedge convention above, all diagonal entries of  $D_V$  and  $D_E$  are strictly positive; isolated nodes, if they occurred, would contribute an  $e_v e_v^\top$  block to  $L_V$ , preserving symmetric positive semidefiniteness.

On the hyperedge side, we define the size-normalised overlap matrix

$$A_E(H) := \text{offdiag}\left(D_E^{-1/2} H^\top H D_E^{-1/2}\right), \quad (3)$$

where  $\text{offdiag}(\cdot)$  sets diagonal entries to zero. Here,  $H^\top H$  counts shared-node overlaps between hyperedges, while the normalisation by  $D_E$  removes the most direct size effect. Writing  $D_{\text{ov}} := \text{diag}(A_E(H)\mathbf{1}_m)$  for the diagonal of overlap-weighted degrees, we then define the *normalised hyperedge-overlap Laplacian*

$$L_E(H) := I_m - D_{\text{ov}}^{-1/2} A_E(H) D_{\text{ov}}^{-1/2}. \quad (4)$$

This is a direct analogue of the symmetric normalised graph Laplacian [14] applied to the weighted overlap graph on hyperedges induced by shared node memberships, closely related to the pairwise reductions used in the spectral analysis of hypergraphs [1; 9] and to the overlap-based operators in Macgregor and Sun [29]. To our knowledge, the size-normalised overlap construction in (3)–(4) is specific to our incidence-space framework; its positive semidefiniteness is established in Lemma A.1. The operator  $L_E(H)$  *smooths signals across hyperedges* with similar node-membership patterns. Together,  $L_V(H)$  and  $L_E(H)$  provide the row-side and column-side geometry of the incidence representation.

### 3 HEDGE: Structured Stochastic Diffusion in Incidence Space

HEDGE is a generative model defined directly on relaxed incidence matrices. The central idea is to combine a hypergraph-specific two-sided heat operator, which encodes incidence-space geometry, with a universal Ornstein–Uhlenbeck mechanism that yields a tractable Gaussian terminal law. This produces a forward diffusion that is hypergraph-adapted near the data, while still admitting well-defined unconditional generation through a learned state-only reverse-drift field (see Figure 1 for an illustration). Full proofs for the results in this section are given in Appendix A.

#### 3.1 Structured heat–OU forward diffusion

**Relaxed incidence matrices.** We work with real-valued matrices  $X \in \mathbb{R}^{n \times m}$  as continuous surrogates for binary incidence matrices  $H \in \{0, 1\}^{n \times m}$ . We refer to such  $X$  as *relaxed incidence matrices*. We use  $s \in [0, S]$  to denote forward noising time, where  $s = 0$  corresponds to the observed hypergraph and larger  $s$  corresponds to progressively more corrupted states; the forward state at time  $s$  is denoted  $X_s$ . For reverse-time generation we use  $t \in [0, S]$ , where  $t = 0$  denotes the initial draw from the base law and  $t = S$  the final generated sample; the reverse state at time  $t$  is denoted  $Y_t$ . Along the reverse trajectory, the forward and reverse times are related by  $s = S - t$ . Given an observed hypergraph with incidence matrix  $H$ , we define the two-sided linear operator

$$\mathcal{A}_H(X) := L_V(H)X + X L_E(H), \quad X \in \mathbb{R}^{n \times m}. \quad (5)$$

This operator smooths the relaxed incidence matrices simultaneously across nodes and across overlapping hyperedges. In particular, if  $\frac{d}{ds} X_s = -\mathcal{A}_H(X_s)$  with  $X_0 = H$ , then  $X_s = e^{-sL_V(H)} H e^{-sL_E(H)}$ : the node-side and hyperedge-side heat kernels act by left and right multiplication, respectively, inducing a natural hypergraph-aware noising mechanism in incidence space.

**Proposition 3.1** (Dissipativity and spectral decoupling of the pure heat operator). *The operator  $\mathcal{A}_H$  is self-adjoint and positive semidefinite with respect to the Frobenius inner product. Consequently, the pure heat flow  $\frac{d}{ds} Z_s = -\mathcal{A}_H(Z_s)$  is dissipative,  $\frac{d}{ds} \|Z_s\|_F^2 = -2\langle Z_s, \mathcal{A}_H(Z_s) \rangle_F \leq 0$ . Moreover, if  $L_V(H) = U\Lambda U^\top$  and  $L_E(H) = VMV^\top$  with eigenvalues  $\{\lambda_i\}$  and  $\{\mu_j\}$ , then the transformed state  $\tilde{Z}_s := U^\top Z_s V$  satisfies  $\frac{d}{ds} \tilde{Z}_s(i, j) = -(\lambda_i + \mu_j)\tilde{Z}_s(i, j)$ , so each joint node–hyperedge mode decays at rate  $\lambda_i + \mu_j$ .*

Proposition 3.1 shows that the two-sided heat operator defines a well-behaved noising mechanism in incidence space: it is dissipative in the Frobenius geometry and admits a joint node–hyperedge spectral decomposition. As a result, the heat flow suppresses higher-frequency incidence modes first, while preserving lower-frequency structure for longer. This gives a natural hypergraph-aware inductive bias, since corruption is guided by the geometry induced by  $L_V(H)$  and  $L_E(H)$  rather than by isotropic noise alone. Proposition 3.1 requires only that  $L_V(H)$  and  $L_E(H)$  be symmetric positive semidefinite, both of which hold under our definitions (see Appendix A.1).

The limitation of pure heat flow is that it contracts toward a hypergraph-dependent low-complexity limit rather than a universal non-degenerate base law. We therefore embed this heat operator (5) within a scheduled stochastic diffusion that gradually transitions to an OU regime.

**Forward noising schedule.** Let  $S > 0$  be a terminal time horizon, let  $M_0 \in \mathbb{R}^{n \times m}$  be a fixed mean matrix independent of the test-time hypergraph, and let  $\gamma > 0$  and  $\tau > 0$  control the late-time OU dynamics. In practice,  $M_0$  specifies the centre of the Gaussian base law used for reverse-time generation. The simplest choice is  $M_0 = 0$ , but data-adapted choices, such as matching the average incidence density, are also possible. Crucially,  $M_0$  is fixed globally and does not depend on the unknown test-time hypergraph. We introduce continuous scheduling functions

$$\alpha, \beta : [0, S] \rightarrow [0, 1], \quad \alpha(s) + \beta(s) = 1, \quad \alpha(0) = 1, \beta(0) = 0, \quad (6)$$

with  $\alpha$  decreasing and  $\beta$  increasing over time, and with  $\beta$  strictly positive on  $(0, S]$ . The forward process on relaxed incidence matrices is then defined by the matrix-valued SDE

$$dX_s = -\alpha(s)\mathcal{A}_H(X_s) ds - \beta(s)\gamma(X_s - M_0) ds + \sqrt{2\tau\beta(s)} dW_s, \quad X_0 = H, \quad (7)$$

where  $W_s$  is matrix Brownian motion with independent standard Brownian entries. At early times,  $\alpha(s) \approx 1$  and  $\beta(s) \approx 0$ , so the dynamics are dominated by the hypergraph-specific two-sided heat operator. As  $s \rightarrow S$ , the heat contribution is gradually suppressed and the OU component becomes dominant. At late times, the dynamics approach the matrix-valued OU process  $dX_s = -\gamma(X_s - M_0)ds + \sqrt{2\tau}dW_s$ , whose terminal law is

$$X_\infty \sim \mathcal{N}(M_0, \frac{\tau}{\gamma}I_{nm}). \quad (8)$$

Hence the process preserves hypergraph-specific structure-aware noising near the data while ensuring an explicit, non-degenerate terminal law independent of the unknown test-time hypergraph. This Gaussian law is then used to initialise reverse-time generation, i.e.  $p(Y_0) = p(X_\infty)$ .

### 3.2 Conditional Gaussian law and the forward process

A key advantage of this forward process is that, conditional on the observed hypergraph, it remains a linear-Gaussian diffusion. This yields an exact perturbation law at every time and hence allows us to train against exact reverse-drift targets rather than Monte Carlo approximations. Vectorising  $x_s := \text{vec}(X_s) \in \mathbb{R}^{nm}$  and using  $\text{vec}(AXB) = (B^\top \otimes A)\text{vec}(X)$ , the SDE (7) becomes

$$dx_s = -B_s(H) x_s ds + \beta(s)\gamma \text{vec}(M_0) ds + \sqrt{2\tau\beta(s)} dw_s, \quad (9)$$

with  $B_s(H) := \alpha(s)(I_m \otimes L_V(H) + L_E(H) \otimes I_n) + \beta(s)\gamma I_{nm}$ , and where we have used symmetry of  $L_E$  to drop the transpose. This is a linear time-inhomogeneous SDE with additive Gaussian noise, so the conditional law of  $x_s$  is Gaussian for every  $s \in [0, S]$  [33; 35].

**Proposition 3.2** (Conditional Gaussian law of the forward process). *For each  $s \in [0, S]$ , the conditional law of the forward state satisfies  $\text{vec}(X_s) | H \sim \mathcal{N}(m_s(H), C_s(H))$ , where*

$$\frac{d}{ds} m_s(H) = -B_s(H) m_s(H) + \beta(s)\gamma \text{vec}(M_0), \quad m_0(H) = \text{vec}(H), \quad (10)$$

$$\frac{d}{ds} C_s(H) = -B_s(H)C_s(H) - C_s(H)B_s(H)^\top + 2\tau\beta(s) I_{nm}, \quad C_0(H) = 0. \quad (11)$$

Under  $\beta > 0$  on  $(0, S]$ ,  $C_s(H)$  is positive definite (hence invertible) for all  $s \in (0, S]$ .

Given a training hypergraph  $H$  and forward time  $s$ , one may solve (10)–(11) and sample  $X_s$  from its conditional Gaussian law (see Appendix A.2 for details). Moreover, for any  $s \in (0, S]$ , the covariance  $C_s(H)$  is invertible by Proposition 3.2, and the exact conditional score is

$$r_{s|H}^*(X) = -\text{mat}(C_s(H)^{-1}(\text{vec}(X) - m_s(H))), \quad (12)$$

which enters directly into the exact conditional reverse drift. This exact conditional reverse drift is only available when the originating hypergraph  $H$  is known; since  $H$  is unknown at generation time, exact conditional supervision does not remove the need to train a state-only reverse field surrogate, but it does provide noiseless training targets for that field.

**Efficient computation.** A naive evaluation of (10)–(11) requires working with  $nm \times nm$  matrices. Proposition 3.1 shows that  $B_s(H)$  is diagonalisable in the Kronecker basis  $U \otimes V$  formed from the eigendecompositions of  $L_V(H)$  and  $L_E(H)$ . In this basis, the mean and covariance ODEs decouple into  $nm$  independent scalar ODEs indexed by eigenmodes  $(i, j)$ , so (10)–(11) can be solved in  $O(nm)$  per step after a one-time  $O(n^3 + m^3)$  eigendecomposition.

### 3.3 Learning the $L^2$ -optimal state-only reverse drift

The forward process (7) is defined conditionally on a training hypergraph  $H$ , so for fixed  $H$ , the reverse-time dynamics are available in closed form. However, these dynamics depend explicitly on  $H$ , which is not available at generation time. The central modelling problem is therefore to construct a reverse-time drift field that can be evaluated without access to the original hypergraph.

**Conditional reverse drift.** Let  $p_{s|H}(X)$  denote the conditional density of the forward diffusion at time  $s$ . Writing

$$b_{s|H}(X) := -\alpha(s)\mathcal{A}_H(X) - \beta(s)\gamma(X - M_0) \quad (13)$$

for the conditional forward drift in (7), the forward SDE then takes the form

$$dX_s = b_{s|H}(X_s) ds + \sqrt{2\tau\beta(s)} dW_s, \quad X_0 = H,$$

with state-independent diffusion coefficient. Under standard regularity conditions on  $\{p_{s|H}\}_{s \in (0, S]}$ , the classical time-reversal formula for diffusions with additive noise [2; 20] then gives the conditional reverse-time drift

$$u_{s|H}^*(X) = -b_{s|H}(X) + 2\tau\beta(s) r_{s|H}^*(X) = \alpha(s)\mathcal{A}_H(X) + \beta(s)\gamma(X - M_0) + 2\tau\beta(s) r_{s|H}^*(X), \quad (14)$$

where  $r_{s|H}^*(X) = \nabla_X \log p_{s|H}(X)$  is the conditional score. Since the forward process is conditionally linear-Gaussian,  $r_{s|H}^*$  is available exactly from (12), and hence  $u_{s|H}^*$  can be evaluated without approximation during training.

**Reverse-drift regression objective.** We learn a time-dependent neural field  $u_s^\theta : \mathbb{R}^{n \times m} \rightarrow \mathbb{R}^{n \times m}$  by regressing directly onto the conditional reverse-drift targets  $u_{s|H}^*(X_s)$ . The population objective is

$$\mathcal{L}(\theta) = \mathbb{E}_{H \sim p_{\text{data}}, s \sim \rho, X_s \sim p_{s|H}} \left[ \|u_s^\theta(X_s) - u_{s|H}^*(X_s)\|_F^2 \right]. \quad (15)$$

**Proposition 3.3** ( $L^2$ -optimal state-only reverse-drift target). *For each fixed  $s$ , the population minimiser of (15) is  $u_s^{L^2}(X) = \mathbb{E} \left[ u_{s|H}^*(X) \mid X_s = X \right]$ . Moreover, this predictor coincides with the marginal reverse drift of the forward process: the marginal density path  $\{\hat{p}_s\}$  is generated by the Markovian state-only drift  $\bar{b}_s(X) = \mathbb{E}[b_{s|H}(X) \mid X_s = X]$ , and its time-reversal yields a state-only drift equal to  $u_s^{L^2}$ .*

Proposition 3.3 shows that the learning target used by HEDGE is the  $L^2$ -optimal state-only approximation to the exact hypergraph-conditioned reverse drift. Equivalently, this target is the reverse drift of the marginal forward process. Decomposing the target,

$$u_s^{L^2}(X) = \alpha(s) \sum_{i=1}^N \pi_s(i \mid X) \mathcal{A}_{H^{(i)}}(X) + \beta(s)\gamma(X - M_0) + 2\tau\beta(s) \nabla_X \log \hat{p}_s(X),$$

the OU and marginal-score terms (second and third) are state-only by construction, but the posterior-averaged structural term does not reduce to a closed-form function of  $X$  alone, due to the dependence on  $H$  — which is why a neural surrogate is required.

**Learned reverse-time SDE.** At generation time we initialise from the Gaussian base law (8) and simulate

$$dY_t = u_{S-t}^\theta(Y_t) dt + \sqrt{2\tau\beta(S-t)} d\bar{W}_t, \quad t \in [0, S]. \quad (16)$$

In the idealised setting, if the learned reverse field matches the  $L^2$ -optimal state-only target exactly and generation is initialised from the exact terminal marginal, then reverse-time sampling recovers the data law exactly; see Appendix A.3. In practice, the key questions are how approximation error in the learned reverse field and numerical discretisation affect the quality of generation.

### 3.4 Stability and generation error

**Theorem 3.4** (Finite-horizon stability in  $W_2$  via one-sided Lipschitz). *Let  $Y_t^*$  and  $Y_t^\theta$  solve the ideal and learned reverse SDEs with the same diffusion coefficient  $\sqrt{2\tau\beta(S-t)}$ , synchronously coupled by the same Brownian motion. Suppose  $u^\theta$  admits a measurable one-sided Lipschitz constant  $\kappa : [0, S] \rightarrow \mathbb{R}$ , i.e.  $\langle X - Y, u_s^\theta(X) - u_s^\theta(Y) \rangle_F \leq \kappa_s \|X - Y\|_F^2$  for all  $X, Y, s$ .*

**Algorithm 1** HEDGE**Training**

- 1: **Input:** data  $\{H^{(i)}\}$ , time law  $\rho$ , step size  $\eta$
- 2: **for** each training iteration **do**
- 3:   Sample  $H \sim p_{\text{data}}$  and  $s \sim \rho$
- 4:   Solve (10)–(11) to get  $m_s(H)$  and  $C_s(H)$
- 5:   Sample  $\xi \sim \mathcal{N}(0, I_{nm})$ , form  
 $X_s \leftarrow \text{mat}(m_s(H) + C_s(H)^{1/2}\xi)$
- 6:   Evaluate target drift  $u^* \leftarrow u_{s|H}^*(X_s)$
- 7:   Compute loss  $\mathcal{L}(\theta) \leftarrow \|u_s^\theta(X_s) - u^*\|_F^2$
- 8:   Update  $\theta \leftarrow \theta - \eta \nabla_\theta \mathcal{L}(\theta)$
- 9: **end for**
- 10: **return** trained reverse field  $u_s^\theta$

**Generation**

- 1: **Input:**  $u_s^\theta$ , schedule  $\beta$ ,  $(M_0, \gamma, \tau)$ , horizon  $S$ ; projection  $\Pi(Y)_{ij} = \mathbf{1}\{Y_{ij} \geq 1/2\}$
- 2: Choose time grid  $0 = t_0 < \dots < t_K = S$
- 3: Initialise  $Y_{t_0} \sim \mathcal{N}(M_0, \frac{\tau}{\gamma} I_{nm})$
- 4: **for**  $k = 0, \dots, K - 1$  **do**
- 5:    $\Delta t \leftarrow t_{k+1} - t_k$ ,  $s_k \leftarrow S - t_k$
- 6:    $\hat{u}_k \leftarrow u_{s_k}^\theta(Y_{t_k})$
- 7:   Sample  $\varepsilon_k \sim \mathcal{N}(0, I_{nm})$
- 8:    $Y_{t_{k+1}} \leftarrow Y_{t_k} + \Delta t \hat{u}_k + \sqrt{2\tau\beta(s_k)\Delta t} \varepsilon_k$
- 9: **end for**
- 10: **return**  $\hat{H} \leftarrow \Pi(Y_{t_K})$

Define

$$\Lambda(t) := \int_0^t (2\kappa_{S-r} + 1) dr, \quad \mathcal{E}_{\text{rev}}(t)^2 := W_2(\nu_0^\theta, \nu_0^*)^2 + \int_0^t e^{-\Lambda(r)} \mathbb{E}[\|u_{S-r}^\theta(Y_r^*) - u_{S-r}^*(Y_r^*)\|_F^2] dr.$$

Then, for every  $t \in [0, S]$ ,

$$W_2(\text{Law}(Y_t^\theta), \text{Law}(Y_t^*)) \leq e^{\Lambda(t)/2} \mathcal{E}_{\text{rev}}(t). \quad (17)$$

Taking  $\kappa_s \equiv L$  recovers the Grönwall prefactor  $e^{(2L+1)t/2}$ . If  $\kappa_s \leq \kappa_* < -1/2$  uniformly on a subinterval bounded away from  $s = 0$ , then the corresponding contribution to  $e^{\Lambda(S)/2}$  is contractive on that subinterval.

Theorem 3.4 shows that reverse-generation error is controlled by a single reverse-process term  $\mathcal{E}_{\text{rev}}(t)$ , which combines both initialisation mismatch and reverse-drift approximation error along the ideal reverse trajectory. The one-sided Lipschitz formulation is useful because it does not require the learned reverse drift to be globally contractive. In reverse time, the structural heat contribution appears with the anti-diffusive sign  $+\alpha(s)\mathcal{A}_H$ , and the term  $+\beta(s)\gamma(X - M_0)$  is expansive before being combined with the score. Contractivity, when it holds, is therefore a property of the full reverse drift, including the score contribution, not of the heat or OU terms separately.

Together with the Euler–Maruyama bound (Corollary A.10 in Appendix A.5), Theorem 3.4 yields the total generation-error decomposition

$$W_2(\text{Law}(\hat{Y}_S^\theta), p_{\text{data}}) \leq C \Delta t^{1/2} + e^{\Lambda(S)/2} \mathcal{E}_{\text{rev}}(S).$$

Thus the final generation error splits into a numerical discretisation term and a reverse-process term, with the latter capturing both initialisation mismatch and reverse-drift approximation error. In the ideal case with exact initialisation, the remaining error is of order  $\Delta t^{1/2}$ . Full details are given in Appendix A.11.

### 3.5 Equivariant reverse-drift model

The learned field should transform consistently under independent permutations of rows and columns, corresponding to relabellings of nodes and hyperedges. We work with the product symmetry group  $S_n \times S_m$ , acting on incidence-space states as  $X \mapsto PXQ^\top$ , where  $P$  and  $Q$  are permutation matrices of sizes  $n \times n$  and  $m \times m$ . We therefore parameterise  $u_s^\theta$  using an  $S_n \times S_m$ -equivariant architecture [30], satisfying

$$u_s^\theta(PXQ^\top) = P u_s^\theta(X) Q^\top. \quad (18)$$

Under the natural symmetry assumptions on the data distribution and forward process, the  $L^2$ -optimal state-only reverse-drift target itself belongs to this symmetry class.

**Proposition 3.5** (Equivariance of the  $L^2$ -optimal target). *Assume the data distribution is invariant under independent row and column permutations, the base mean  $M_0$  is permutation-invariant, and the driving Brownian motion is isotropic. The operators  $L_V$  and  $L_E$  transform equivariantly under  $H \mapsto PHQ^\top$  by direct computation from their definitions. Then the forward operator  $\mathcal{A}_H$  is  $S_n \times S_m$ -equivariant, the conditional forward law and conditional reverse drift transform equivariantly, and the  $L^2$ -optimal state-only reverse-drift target satisfies  $u_s^{L^2}(PXQ^\top) = P u_s^{L^2}(X) Q^\top$ .*

Ablation	Intersect. WD	Tail gap	Node spec. WD	Edge spec. WD	Feature MMD
Full HEDGE	<b>0.105 ± 0.076</b>	<b>0.012 ± 0.004</b>	<b>0.034 ± 0.020</b>	<b>0.036 ± 0.027</b>	<b>0.331 ± 0.258</b>
OU only	0.132 ± 0.080	<i>0.012 ± 0.006</i>	0.044 ± 0.020	0.039 ± 0.030	0.391 ± 0.296
Node only	0.137 ± 0.086	0.019 ± 0.006	0.036 ± 0.021	<i>0.036 ± 0.030</i>	<i>0.353 ± 0.311</i>
Edge only	<i>0.126 ± 0.079</i>	0.014 ± 0.004	<i>0.034 ± 0.022</i>	0.037 ± 0.030	0.373 ± 0.279

Table 1: Simulated-data ablations. Values are mean  $\pm$  standard error after averaging over synthetic datasets. Lower is better for all columns; best values are **bold** and second-best values are in *italics*.

## 4 Related Work

**Hypergraph generation.** Hypergraph generation has been studied through statistical and mechanistic approaches. Classical random, configuration-style, and latent-structure models prescribe higher-order marginals or impose structured dependence through rewiring, latent variables, or block structure [12; 13; 19; 41]. More recent learned generators include mechanistic sequence-based models and diffusion-style approaches [15; 18; 44]. In particular, HYGENE [18] performs diffusion on a graph-like bipartite encoding of the hypergraph, while DDE [44] generates hyperlinks by diffusing latent hyperlink embeddings. HEDGE differs from these approaches by operating directly on relaxed incidence matrices, so node–hyperedge participation is modelled in its native rectangular representation rather than through a graph reduction or latent hyperlink embedding.

**Heat diffusion and spectral structure on hypergraphs.** Our forward process is built from spectral operators on hypergraphs. On the node side, we use the normalised hypergraph Laplacian of Zhou et al. [47] and Chan et al. [9]. More broadly, Laplacian heat flow has recently been used as a structure-aware noising mechanism in graph generation [39]. The limitation of pure heat flow, however, is that it contracts toward a data-dependent low-complexity limit rather than a universal non-degenerate terminal law. HEDGE addresses this by incorporating an Ornstein–Uhlenbeck component, thus yielding structure-aware noising together with an explicit Gaussian base law.

**Reverse-time generative modelling.** HEDGE has natural connections to score-based diffusion models [22; 38]. Unlike standard score-based models, whose reverse dynamics are parameterised by the marginal score of a fixed forward perturbation, our forward process is conditioned on the observed hypergraph. The exact reverse drift therefore contains both a score term and hypergraph-specific structural terms, so a score-only parameterisation is insufficient. We instead learn a state-only reverse drift by regressing onto exact conditional reverse-drift targets, closer in spirit to vector-field regression methods such as flow matching and generator matching [28; 23; 39].

## 5 Experiments

We evaluate HEDGE in two ways. First, controlled synthetic ablations test the modelling choices behind the structured heat–OU process and the two-sided incidence operator. Second, a matched real-data benchmark compares HEDGE with statistical and learned hypergraph generators across six datasets. We focus in the main text on higher-order structural diagnostics, with fuller metric definitions, calibration results, and additional qualitative examples deferred to Appendix B.

### 5.1 Experimental setup

**Task and representation.** Since many real datasets consist of a single large observed hypergraph, we evaluate generation on *fixed-size subhypergraphs*: from each observed hypergraph we sample a bank of fixed-size subhypergraphs, train on one subset, and compare generated samples with held-out subhypergraphs of the same size. This gives a controlled test of whether a method reproduces higher-order incidence structure at fixed node–hyperedge dimension. Although this benchmark fixes size within each dataset, HEDGE itself operates on rectangular incidence matrices and is not tied to one global size. After reverse-time sampling in relaxed incidence space, we project to a binary incidence matrix using the map  $\Pi$  in Algorithm 1; in all experiments,  $\Pi$  is entrywise thresholding at  $1/2$ , i.e.  $\Pi(Y)_{ij} = \mathbf{1}\{Y_{ij} \geq 1/2\}$ . This projection is stable in practice: 99.34% of relaxed entries lie within 0.10 of either 0 or 1, so the choice of threshold within  $[0.1, 0.9]$  has negligible effect on outputs. All experiments were run on a MacBook Pro with an Apple M4 Pro chip and 24GB memory.

**Datasets.** The real-data study uses six datasets: CORA, CITESEER, ACTOR, HOUSE-COMMITTEES, DBLP, and TWITCH. They span sparse citation-like incidence structure (CORA, CITESEER, DBLP), broader co-membership

regimes (ACTOR, TWITCH), and highly heterogeneous committee overlap (HOUSE-COMMITTEES). Dataset details are given in Appendix B.1.

**Comparators.** We compare four methods under the same fixed-size protocol: HEDGE, HCM-MCMC [12], ER-HG, and HYGENE [18]. HCM-MCMC is a strong configuration-style baseline that directly targets degree and size structure; ER-HG is an Erdős-Rényi-style random hypergraph baseline; and HYGENE is a learned diffusion-based hypergraph generator. All methods use the same dataset/seed splits and metric pipeline. Real-data results are reported over 10 independent seeds.

**Metrics.** The main table emphasises metrics that probe higher-order structure: (i) *Overlap Tail Gap*; (ii) *Intersection WD*; and (iii) *Feature MMD*. Lower is better in all cases. These metrics complement the calibration and marginal-distribution results in Appendix B.4, including density, mean hyperedge size, mean node degree, and Wasserstein distances for size and degree distributions. Full definitions of each metric are given in Appendix B.2.

## 5.2 Ablation study

We use simulated hypergraph distributions to isolate the main modelling choices in HEDGE. The ablations test whether structured heat improves over unstructured OU noising, and whether using both sides of the incidence geometry is preferable to smoothing only across nodes or only across hyperedges. *Full* HEDGE combines structured heat, the OU terminal mechanism, and both node- and hyperedge-side geometry. *OU only* removes the heat term; *Node only* keeps only  $L_V(H)X$ ; and *Edge only* keeps only  $XL_E(H)$ . Table 1 reports averages across synthetic regimes; full per-dataset tables are in Appendix B.3.

The ablations support the structured incidence-space construction. Full HEDGE is best on all five reported metrics. OU-only is worse except for a near-tie on Tail gap, suggesting that unstructured OU corruption may match a local overlap-tail statistic but fails to reproduce the broader overlap distribution, spectra, and feature-space structure as well. The one-sided variants are competitive on individual metrics, with Edge only second-best on Intersection WD and Node only second-best on Feature MMD, but neither matches the overall balance of the full model. Thus the heat-OU process with both node- and hyperedge-side smoothing gives the most consistent performance on the higher-order diagnostics that motivate HEDGE.

## 5.3 Real-data comparisons

The main empirical result is a matched real-data comparison across CORA, CITESEER, ACTOR, HOUSE-COMMITTEES, DBLP, and TWITCH. Table 2 reports the higher-order metrics most aligned with the goal of incidence-space hypergraph generation; calibration and marginal-distribution results are given in Appendix B.

HEDGE is the strongest method on the overlap-sensitive criteria that distinguish genuine hypergraph generation from marginal matching. It achieves the best Intersection WD on all six datasets, showing that it most accurately reproduces the full distribution of pairwise hyperedge intersections. It also gives the best Overlap Tail Gap on five of six datasets and is tied with HCM-MCMC on CITESEER. On Feature MMD, HEDGE is best on five datasets and second only to HCM-MCMC on CORA. This is a stronger conclusion than aggregate competitiveness: HEDGE is consistently best precisely on the metrics that measure higher-order overlap structure.

The comparison with HCM-MCMC is especially informative. Configuration-style models are designed to preserve degree and size behaviour, and Appendix B.4 confirms that HCM-MCMC is often highly competitive on these marginal quantities. However, Table 2 shows that matching such marginals is not enough to reproduce higher-order incidence representation: HEDGE improves the overlap distribution and multivariate structural discrepancy across the real benchmarks. Figure 2 (right) shows a representative held-out comparison on HOUSE-COMMITTEES. The native hypergraph rendering illustrates the same pattern as the quantitative results: HEDGE better preserves the broad incidence pattern and overlap organisation, whereas the weaker baselines either homogenise the incidence structure or produce visibly implausible occupancy. This qualitative example is not used as evidence in place of the metrics, but it helps explain why the overlap-sensitive diagnostics favour HEDGE. Additional qualitative examples are given in Appendix B.5.

## 6 Limitations and Future Work

HEDGE is a first step toward diffusion-based hypergraph generation directly in incidence space, and several limitations remain. Our empirical protocol uses fixed-size subhypergraphs, which gives a controlled comparison at matched node-hyperedge dimensions but does not address fully variable-size generation. The current model also generates unweighted, unattributed incidence matrices; extensions to attributes, weights, timestamps, or typed relations would require additional mixed discrete-continuous modelling and evaluation.

Metric	Method	Cora	CiteSeer	Actor	H.-Comm.	DBLP	Twitch
Overlap Tail Gap	HEDGE	<b>0.005</b>	0.012	<b>0.004</b>	<b>0.034</b>	<b>0.011</b>	<b>0.008</b>
	HCM-MCMC	<i>0.006</i>	<i>0.012</i>	<i>0.008</i>	<i>0.035</i>	0.016	<i>0.018</i>
	ER-HG	0.006	<b>0.005</b>	0.032	0.130	<i>0.012</i>	0.023
	HYGENE	0.618	0.738	0.992	0.419	0.977	0.980
Intersection WD	HEDGE	<b>0.017</b>	<b>0.050</b>	<b>0.041</b>	<b>0.223</b>	<b>0.080</b>	<b>0.075</b>
	HCM-MCMC	<i>0.026</i>	<i>0.081</i>	<i>0.058</i>	<i>0.320</i>	<i>0.081</i>	<i>0.113</i>
	ER-HG	0.167	0.187	0.319	0.612	0.295	0.334
	HYGENE	4.39	21.65	61.56	3.25	40.13	62.61
Feature MMD	HEDGE	<i>0.123</i>	<b>0.053</b>	<b>0.136</b>	<b>0.072</b>	<b>0.083</b>	<b>0.101</b>
	HCM-MCMC	<b>0.110</b>	<i>0.194</i>	<i>0.277</i>	<i>0.163</i>	<i>0.102</i>	<i>0.159</i>
	ER-HG	1.06	1.08	0.928	0.699	0.951	0.932
	HYGENE	0.524	0.802	1.01	0.422	0.999	0.890

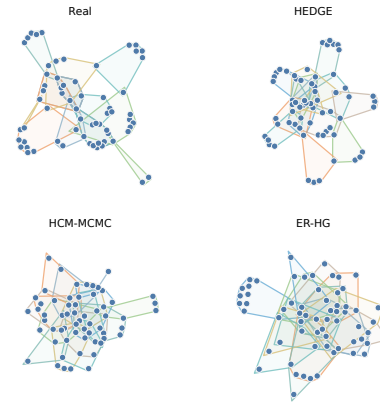


Figure 2: Real-data comparisons. Left: higher-order metrics across real hypergraph datasets. Lower is better for all metrics; best values are **bold** and second-best values are in *italics*. H.-Comm. denotes House Committees. Right: qualitative hypergraph comparison on House-Committees, showing a real data hypergraph alongside generated hypergraphs from HEDGE, HCM-MCMC, and ER-HG.

There are also computational and modelling limitations. The conditional Gaussian targets rely on spectral operators computed from each observed hypergraph; although the Kronecker structure is feasible for our benchmarks, larger hypergraphs will require approximate spectral or local operator methods. The final projection from relaxed samples to binary incidence matrices is simple thresholding, which works well empirically but does not explicitly enforce constraints such as non-empty hyperedges, absence of isolated nodes, or prescribed sparsity. Finally, configuration-style baselines remain strong on degree and hyperedge-size marginals because they target those quantities directly. Future work should explore combining incidence-space diffusion with explicit degree/size conditioning, constrained projection, and sharper statistical theory for learned reverse drifts.

## References

- [1] Sameer Agarwal, Kristin Branson, and Serge Belongie. Higher order learning with graphs. In *Proceedings of the 23rd International Conference on Machine Learning (ICML)*, 2006.
- [2] Brian D. O. Anderson. Reverse-time diffusion equation models. *Stochastic Processes and their Applications*, 12(3):313–326, 1982.
- [3] Federico Battiston, Giulia Cencetti, Iacopo Iacopini, Vito Latora, Maxime Lucas, Alice Patania, Jean-Gabriel Young, and Giovanni Petri. Networks beyond pairwise interactions: Structure and dynamics. *Physics Reports*, 874:1–92, 2020.
- [4] Austin R. Benson, Rediet Abebe, Michael T. Schaub, Ali Jadbabaie, and Jon Kleinberg. Simplicial closure and higher-order link prediction. *Proceedings of the National Academy of Sciences*, 115(48):E11221–E11230, 2018.
- [5] Patrick Billingsley. *Probability and Measure*. Wiley, New York, 3 edition, 1995.
- [6] Damiano Brigo. The general mixture-diffusion sde and its relationship with an uncertain-volatility option model with volatility-asset decorrelation. *arXiv preprint arXiv:0812.4052*, 2008.
- [7] Alberto Cabezas and Christopher Nemeth. Transport elliptical slice sampling. In *International Conference on Artificial Intelligence and Statistics*, pages 3664–3676. PMLR, 2023.
- [8] Patrick Cattiaux, Giovanni Conforti, Ivan Gentil, and Christian Léonard. Time reversal of diffusion processes under a finite entropy condition. *Annales de l’Institut Henri Poincaré, Probabilités et Statistiques*, 59(4):1844–1881, 2023.
- [9] Timothy H. Chan, Anand Louis, and Zhihao Gavin Tang. Spectral properties of hypergraph laplacians and applications. *Journal of the ACM*, 65(4), 2018.
- [10] Sinho Chewi, Jonathan Niles-Weed, and Philippe Rigollet. *Statistical optimal transport*. Springer, 2025.
- [11] Eli Chien, Chao Pan, Jianhao Peng, and Olgica Milenkovic. You are AllSet: a multiset function framework for hypergraph neural networks. In *International Conference on Learning Representations (ICLR)*, 2022.
- [12] Philip S. Chodrow. Configuration models of random hypergraphs. *Journal of Complex Networks*, 8(3):cnaa018, 2020.

- [13] Philip S. Chodrow, Nate Veldt, and Austin R. Benson. Generative hypergraph clustering: from blockmodels to modularity. *Science Advances*, 7(28), 2021.
- [14] Fan RK Chung. *Spectral graph theory*, volume 92. American Mathematical Soc., 1997.
- [15] Manh Tuan Do, Se-eun Yoon, Bryan Hooi, and Kijung Shin. Structural patterns and generative models of real-world hypergraphs. In *Proceedings of the 26th ACM SIGKDD International Conference on Knowledge Discovery and Data Mining*, pages 176–186, 2020.
- [16] Leo L Duan. Transport monte carlo: High-accuracy posterior approximation via random transport. *Journal of the American Statistical Association*, 118(543):1659–1670, 2023.
- [17] Paul Fearnhead, Christopher Nemeth, Chris J. Oates, and Chris Sherlock. *Scalable Monte Carlo for Bayesian Learning*. Institute of Mathematical Statistics Monographs. Cambridge University Press, 2025.
- [18] Dorian Gailhard, Enzo Tartaglione, Lirida Naviner, and Jhony H Giraldo. Hygene: A diffusion-based hypergraph generation method. In *Proceedings of the AAAI Conference on Artificial Intelligence*, volume 39, pages 16682–16690, 2025.
- [19] Debarghya Ghoshdastidar and Ambedkar Dukkipati. Consistency of spectral hypergraph partitioning under planted partition model. *The Annals of Statistics*, 45(1):289–315, 2017.
- [20] Ulrich G Haussmann and Etienne Pardoux. Time reversal of diffusions. *The Annals of Probability*, pages 1188–1205, 1986.
- [21] Desmond J. Higham. An algorithmic introduction to numerical simulation of stochastic differential equations. *SIAM Review*, 43(3):525–546, 2001.
- [22] Jonathan Ho, Ajay Jain, and Pieter Abbeel. Denoising diffusion probabilistic models. *Advances in Neural Information Processing Systems*, 33:6840–6851, 2020.
- [23] Peter Holderrieth, Marton Havasi, Jason Yim, Neta Shaul, Itai Gat, Tommi Jaakkola, Brian Karrer, Ricky T. Q. Chen, and Yaron Lipman. Generator matching: Generative modeling with arbitrary markov processes. In *The Thirteenth International Conference on Learning Representations*, 2025.
- [24] Steffen Klamt, Utz-Uwe Haus, and Fabian Theis. Hypergraphs and cellular networks. *PLoS Computational Biology*, 5(5), 2009.
- [25] Peter E. Kloeden and Eckhard Platen. *Numerical Solution of Stochastic Differential Equations*. Applications of Mathematics. Springer, 1992.
- [26] Fan Li, Xiaoyang Wang, Wenjie Zhang, Ying Zhang, and Xuemin Lin. DHG-bench: A comprehensive benchmark for deep hypergraph learning. In *The Fourteenth International Conference on Learning Representations*, 2026.
- [27] Ming Li, Yongchun Gu, Yi Wang, Yujie Fang, Lu Bai, Xiaosheng Zhuang, and Pietro Liò. When hypergraph meets heterophily: New benchmark datasets and baseline. *Proceedings of the AAAI Conference on Artificial Intelligence*, 39(17):18377–18384, Apr. 2025.
- [28] Yaron Lipman, Ricky T. Q. Chen, Heli Ben-Hamu, Maximilian Nickel, and Matthew Le. Flow matching for generative modeling. In *International Conference on Learning Representations*, 2023.
- [29] Peter Macgregor and He Sun. Finding bipartite components in hypergraphs. In *Advances in Neural Information Processing Systems (NeurIPS)*, 2021.
- [30] Haggai Maron, Heli Ben-Hamu, Nadav Shamir, and Yaron Lipman. Invariant and equivariant graph networks. In *International Conference on Learning Representations*, 2019.
- [31] Karolis Martinkus, Andreas Loukas, Nathanaël Perraudin, and Roger Wattenhofer. Spectre: Spectral conditioning helps to overcome the expressivity limits of one-shot graph generators. In *International Conference on Machine Learning*, pages 15159–15179. PMLR, 2022.
- [32] M. E. J. Newman. The structure of scientific collaboration networks. *PNAS*, 98(2):404–409, 2001.
- [33] Bernt Øksendal. Stochastic differential equations. In *Stochastic differential equations: an introduction with applications*. Springer, 2000.
- [34] Thomas Pinder, Kathryn Turnbull, Christopher Nemeth, and David Leslie. Gaussian processes on hypergraphs. *arXiv preprint arXiv:2106.01982*, 2021.
- [35] Simo Särkkä and Arno Solin. *Applied Stochastic Differential Equations*. Cambridge University Press, 2019.
- [36] Steven L Scott, Alexander W Blocker, Fernando V Bonassi, Hugh A Chipman, Edward I George, and Robert E McCulloch. Bayes and big data: The consensus monte carlo algorithm. In *Big Data and Information Theory*, pages 8–18. Routledge, 2022.

- [37] Louis Sharrock, Daniel Dodd, and Christopher Nemeth. Tuning-free maximum likelihood training of latent variable models via coin betting. In *International Conference on Artificial Intelligence and Statistics*, pages 1810–1818. PMLR, 2024.
- [38] Yang Song, Jascha Sohl-Dickstein, Diederik P. Kingma, Abhishek Kumar, Stefano Ermon, and Ben Poole. Score-based generative modeling through stochastic differential equations. In *International Conference on Learning Representations (ICLR)*, 2021.
- [39] Anthony Stephenson, Ian Gallagher, and Christopher Nemeth. Generator-based graph generation via heat diffusion. *arXiv preprint arXiv:2602.03612*, 2026.
- [40] Jie Tang, Jimeng Sun, Chi Wang, and Zi Yang. Social influence analysis in large-scale networks. In *Proceedings of the 15th ACM SIGKDD international conference on Knowledge discovery and data mining*, pages 807–816, 2009.
- [41] Kathryn Turnbull, Simón Lunagómez, Christopher Nemeth, and Edoardo Airoldi. Latent space modeling of hypergraph data. *Journal of the American Statistical Association*, 119(548):2634–2646, 2024.
- [42] Clement Vignac, Igor Krawczuk, Antoine Siraudin, Bohan Wang, Volkan Cevher, and Pascal Frossard. Digress: Discrete denoising diffusion for graph generation. In *The Eleventh International Conference on Learning Representations*, 2023.
- [43] Callum Vyner, Christopher Nemeth, and Chris Sherlock. Swiss: A scalable markov chain monte carlo divide-and-conquer strategy. *Stat*, 12(1):e523, 2023.
- [44] Shihao Wu, Junyi Yang, Gongjun Xu, and Ji Zhu. Denoising diffused embeddings: A generative approach for hypergraphs. *arXiv preprint arXiv:2501.01541*, 2025.
- [45] Naganand Yadati, Madhav Nimishakavi, Prateek Yadav, Vikram Nitin, Anand Louis, and Partha Talukdar. Hypergen: A new method for training graph convolutional networks on hypergraphs. In *Advances in Neural Information Processing Systems*, volume 32, 2019.
- [46] Qin Yiming, Manuel Madeira, Dorina Thanou, and Pascal Frossard. Defog: Discrete flow matching for graph generation. In *Forty-second International Conference on Machine Learning*, 2025.
- [47] Dengyong Zhou, Jiayuan Huang, and Bernhard Schölkopf. Learning with hypergraphs: Clustering, classification, and embedding. *Advances in Neural Information Processing Systems*, 19, 2006.

## A Proofs of Theoretical Results

This appendix contains the main theoretical results underpinning the structured heat–OU diffusion used by HEDGE. The development proceeds in five steps. First, we analyse the pure heat component as a two-sided dissipative semigroup. Second, we establish the conditional linear-Gaussian structure of the forward process. Third, we characterise the exact conditional reverse drift and prove that the marginal drift of the forward process coincides with the  $L^2$ -optimal state-only target. Fourth, we prove the finite-horizon stability results under a one-sided Lipschitz  $W_2$  bound and the Euler–Maruyama discretisation bound. Finally, we show that the  $L^2$ -optimal state-only target is  $S_n \times S_m$ -equivariant.

Throughout, we equip  $\mathbb{R}^{n \times m}$  with the Frobenius inner product  $\langle X, Y \rangle_F := \text{tr}(X^\top Y)$  and norm  $\|X\|_F^2 := \langle X, X \rangle_F$ . Inverse degree matrices are interpreted entrywise on strictly positive diagonal entries, with zero on zero diagonal entries.

### A.1 The pure heat operator as a dissipative semigroup

**Lemma A.1** (Positive semidefiniteness of  $L_E$ ). *Fix  $H \in \{0, 1\}^{n \times m}$ . Then  $A_E(H)$  is symmetric and entrywise nonnegative, and  $L_E(H) = I_m - D_{\text{ov}}^{-1/2} A_E(H) D_{\text{ov}}^{-1/2}$  is symmetric positive semidefinite.*

*Proof.* Let  $M := D_E^{-1/2} H^\top H D_E^{-1/2}$ ; since  $H^\top H$  is symmetric and  $D_E^{-1/2}$  is diagonal,  $M$  is symmetric, so  $A_E(H) = \text{offdiag}(M)$  is symmetric. For  $1 \leq i, j \leq m$ ,  $(H^\top H)_{ij} = \sum_v H_{v,i} H_{v,j} = |e_i \cap e_j| \geq 0$ , so  $M$  is entrywise nonnegative; offdiag preserves entrywise nonnegativity, hence so is  $A_E(H)$ .

For positive semidefiniteness, fix  $x \in \mathbb{R}^m$  and partition the indices as  $\mathcal{I}_0 := \{i : \delta_i = 0\}$  and  $\mathcal{I}_+ := \{i : \delta_i > 0\}$ , where  $\delta_i := (D_{\text{ov}})_{ii} = \sum_j A_E(H)_{ij}$ . For  $i \in \mathcal{I}_0$ , nonnegativity of  $A_E(H)$  entrywise forces  $A_E(H)_{ij} = A_E(H)_{ji} = 0$  for all  $j$ , so row and column  $i$  contribute nothing to any quadratic form involving  $A_E(H)$ . Moreover, under our convention  $(D_{\text{ov}}^{-1/2})_{ii} = 0$  whenever  $\delta_i = 0$ , so the  $i$ th row and column of  $D_{\text{ov}}^{-1/2} A_E(H) D_{\text{ov}}^{-1/2}$  are identically zero as well. Writing

$$x^\top L_E(H) x = x^\top x - x^\top D_{\text{ov}}^{-1/2} A_E(H) D_{\text{ov}}^{-1/2} x,$$

the second term therefore reduces to a sum over  $\mathcal{I}_+ \times \mathcal{I}_+$ . Setting  $y_i := x_i/\sqrt{\delta_i}$  for  $i \in \mathcal{I}_+$ ,

$$x^\top D_{\text{ov}}^{-1/2} A_E(H) D_{\text{ov}}^{-1/2} x = \sum_{i,j \in \mathcal{I}_+} A_E(H)_{ij} y_i y_j.$$

For the first term, splitting the sum over  $\mathcal{I}_0 \cup \mathcal{I}_+$  and using  $x_i^2 = \delta_i y_i^2$  on  $\mathcal{I}_+$  gives

$$x^\top x = \sum_{i \in \mathcal{I}_0} x_i^2 + \sum_{i \in \mathcal{I}_+} \delta_i y_i^2 = \sum_{i \in \mathcal{I}_0} x_i^2 + \sum_{i \in \mathcal{I}_+} \left( \sum_{j \in \mathcal{I}_+} A_E(H)_{ij} \right) y_i^2,$$

where the second equality uses  $\delta_i = \sum_{j \in \mathcal{I}_+} A_E(H)_{ij}$  for  $i \in \mathcal{I}_+$  (the terms with  $j \in \mathcal{I}_0$  vanish by the argument above). Combining,

$$x^\top L_E(H) x = \sum_{i \in \mathcal{I}_0} x_i^2 + \sum_{i,j \in \mathcal{I}_+} A_E(H)_{ij} (y_i^2 - y_i y_j).$$

By symmetry of  $A_E(H)$ , the second sum equals  $\frac{1}{2} \sum_{i,j \in \mathcal{I}_+} A_E(H)_{ij} (y_i^2 + y_j^2 - 2y_i y_j) = \frac{1}{2} \sum_{i,j \in \mathcal{I}_+} A_E(H)_{ij} (y_i - y_j)^2$ . Therefore

$$x^\top L_E(H) x = \sum_{i \in \mathcal{I}_0} x_i^2 + \frac{1}{2} \sum_{i,j \in \mathcal{I}_+} A_E(H)_{ij} (y_i - y_j)^2,$$

and both terms are nonnegative because  $A_E(H)$  is entrywise nonnegative, proving  $L_E(H) \succeq 0$ .  $\square$

*Proof of Proposition 3.1.* Write  $L_V := L_V(H)$  and  $L_E := L_E(H)$ , both symmetric PSD (the former by construction and our no-isolated-node convention, the latter by Lemma A.1).

*Self-adjointness:* For  $X, Y \in \mathbb{R}^{n \times m}$ ,  $\langle X, \mathcal{A}_H(Y) \rangle_F = \text{tr}(X^\top L_V Y) + \text{tr}(X^\top Y L_E)$ . Using symmetry of  $L_V, L_E$ ,  $\text{tr}(X^\top L_V Y) = \text{tr}((L_V X)^\top Y)$  and  $\text{tr}(X^\top Y L_E) = \text{tr}((X L_E)^\top Y)$ , giving  $\langle X, \mathcal{A}_H(Y) \rangle_F = \langle \mathcal{A}_H(X), Y \rangle_F$ .

*PSD:*  $\langle X, \mathcal{A}_H(X) \rangle_F = \text{tr}(X^\top L_V X) + \text{tr}(X L_E X^\top) \geq 0$  since  $L_V, L_E \succeq 0$ .

*Dissipativity:* If  $\dot{Z}_s = -\mathcal{A}_H(Z_s)$  then  $\frac{d}{ds} \|Z_s\|_F^2 = -2\langle Z_s, \mathcal{A}_H(Z_s) \rangle_F \leq 0$ .

*Spectral decoupling:* Write  $L_V = U \Lambda U^\top$ ,  $L_E = V M V^\top$  with orthogonal  $U, V$  and diagonal  $\Lambda, M$ . Set  $\tilde{Z}_s := U^\top Z_s V$ . Then

$$\frac{d}{ds} \tilde{Z}_s = -U^\top (L_V Z_s + Z_s L_E) V = -\Lambda \tilde{Z}_s - \tilde{Z}_s M,$$

so entrywise  $\frac{d}{ds} \tilde{Z}_s(i, j) = -(\lambda_i + \mu_j) \tilde{Z}_s(i, j)$ , giving  $\tilde{Z}_s(i, j) = e^{-s(\lambda_i + \mu_j)} \tilde{Z}_0(i, j)$  and  $Z_s = e^{-s L_V} Z_0 e^{-s L_E}$ .  $\square$

**Corollary A.2** (Pure-heat limit). *Let  $Z_s$  satisfy  $\frac{d}{ds} Z_s = -\mathcal{A}_H(Z_s)$  with  $Z_0 \in \mathbb{R}^{n \times m}$ . Then  $Z_s \rightarrow \Pi_V Z_0 \Pi_E$  as  $s \rightarrow \infty$ , where  $\Pi_V$  and  $\Pi_E$  are the orthogonal projections onto  $\ker L_V(H)$  and  $\ker L_E(H)$ , respectively. Moreover, letting*

$$\eta := \min\{\lambda_i + \mu_j : \lambda_i + \mu_j > 0\} > 0,$$

*the convergence is exponential at rate  $\eta$ :*

$$\|Z_s - \Pi_V Z_0 \Pi_E\|_F \leq e^{-\eta s} \|Z_0\|_F \quad \text{for all } s \geq 0.$$

*Proof.* Write  $L_V(H) = U \Lambda U^\top$  and  $L_E(H) = V M V^\top$  with orthogonal  $U, V$  and diagonal  $\Lambda = \text{diag}(\lambda_1, \dots, \lambda_n)$ ,  $M = \text{diag}(\mu_1, \dots, \mu_m)$ ; by Proposition 3.1,  $\lambda_i, \mu_j \geq 0$ . Let  $\Pi_\Lambda \in \mathbb{R}^{n \times n}$  be the diagonal matrix with  $(\Pi_\Lambda)_{ii} = 1$  if  $\lambda_i = 0$  and 0 otherwise, and similarly  $\Pi_M \in \mathbb{R}^{m \times m}$  with  $(\Pi_M)_{jj} = \mathbf{1}[\mu_j = 0]$ . Then  $\Pi_V = U \Pi_\Lambda U^\top$  and  $\Pi_E = V \Pi_M V^\top$  are the orthogonal projections onto  $\ker L_V(H)$  and  $\ker L_E(H)$ .

Setting  $\tilde{Z}_s := U^\top Z_s V$ , Proposition 3.1 gives  $\tilde{Z}_s(i, j) = e^{-s(\lambda_i + \mu_j)} \tilde{Z}_0(i, j)$  entrywise. Split the indices into  $\mathcal{K} := \{(i, j) : \lambda_i + \mu_j = 0\}$  (equivalently,  $\lambda_i = \mu_j = 0$  since both are nonnegative) and its complement  $\mathcal{K}^c$ . For  $(i, j) \in \mathcal{K}$ ,  $\tilde{Z}_s(i, j) = \tilde{Z}_0(i, j)$  for all  $s$ ; for  $(i, j) \in \mathcal{K}^c$ ,  $|\tilde{Z}_s(i, j)| \leq e^{-\eta s} |\tilde{Z}_0(i, j)|$  by definition of  $\eta$ . Hence

$$\|\tilde{Z}_s - \Pi_\Lambda \tilde{Z}_0 \Pi_M\|_F^2 = \sum_{(i,j) \in \mathcal{K}^c} |\tilde{Z}_s(i, j)|^2 \leq e^{-2\eta s} \sum_{(i,j) \in \mathcal{K}^c} |\tilde{Z}_0(i, j)|^2 \leq e^{-2\eta s} \|\tilde{Z}_0\|_F^2.$$

Since  $U, V$  are orthogonal,  $\|\tilde{Z}_s - \Pi_\Lambda \tilde{Z}_0 \Pi_M\|_F = \|Z_s - \Pi_V Z_0 \Pi_E\|_F$  and  $\|\tilde{Z}_0\|_F = \|Z_0\|_F$ , so  $\|Z_s - \Pi_V Z_0 \Pi_E\|_F \leq e^{-\eta s} \|Z_0\|_F$ . Taking  $s \rightarrow \infty$  gives  $Z_s \rightarrow \Pi_V Z_0 \Pi_E$ .  $\square$

## A.2 Conditional Gaussian structure of the forward process

*Proof of Proposition 3.2.* Applying the definition  $\text{vec}(AXB) = (B^\top \otimes A) \text{vec}(X)$  to  $\mathcal{A}_H(X) = L_V X + X L_E$  with symmetric  $L_E$  gives  $\text{vec}(\mathcal{A}_H(X)) = (I_m \otimes L_V + L_E \otimes I_n) \text{vec}(X)$ . The forward SDE therefore becomes

$$dx_s = -B_s(H)x_s ds + b_s ds + \sqrt{2\tau\beta(s)} dw_s, \quad x_0 = \text{vec}(H),$$

with  $b_s = \beta(s)\gamma \text{vec}(M_0)$ , a linear time-inhomogeneous SDE with additive Gaussian noise. Let  $\Phi(s, u; H)$  be the transition matrix of  $\partial_s z_s = -B_s(H)z_s$ , i.e. the unique invertible solution of  $\partial_s \Phi(s, u; H) = -B_s(H)\Phi(s, u; H)$ , with  $\Phi(u, u; H) = I_{nm}$ .

Setting  $y_s := \Phi(0, s; H)x_s$  and applying the product rule,

$$dy_s = \Phi(0, s; H)b_s ds + \sqrt{2\tau\beta(s)}\Phi(0, s; H) dw_s,$$

so integrating and inverting gives

$$x_s = \Phi(s, 0; H) \text{vec}(H) + \int_0^s \Phi(s, u; H)b_u du + \sqrt{2\tau} \int_0^s \Phi(s, u; H)\sqrt{\beta(u)} dw_u.$$

The first two terms are deterministic given  $H$ , and the Wiener integral has deterministic integrand, and hence is a centred Gaussian [35, Sec. 4.3, 5.5, 6.1]. The mean and covariance ODEs (10)–(11) then follow by differentiating the explicit expressions [35, Sec. 5.5, 6.1].

For invertibility of  $C_s(H)$ :  $C_s(H) = 2\tau \int_0^s \beta(u)\Phi(s, u; H)\Phi(s, u; H)^\top du$ . Since  $\beta > 0$  on  $(0, s]$  and  $\Phi$  is invertible, the integrand is positive definite on a set of positive Lebesgue measure, so  $C_s(H) \succ 0$  for all  $s \in (0, S]$ .  $\square$

## A.3 Reverse-time drift and $L^2$ -optimal target

We first give the form of the marginal forward drift under the empirical data measure, which is later used to identify the  $L^2$ -optimal state-only target with a state-only marginal reverse drift.

**Lemma A.3** (Marginal forward drift). *Let  $\hat{p}_{\text{data}} = \frac{1}{N} \sum_i \delta_{H^{(i)}}$  be the empirical data measure. For each  $s \in (0, S]$ , the conditional law  $p_{s|H^{(i)}}$  is a non-degenerate Gaussian by Proposition 3.2, hence strictly positive and  $C^\infty$  in  $X$ , with locally bounded first derivatives uniformly in  $i$ . Under these conditions, the marginal forward process under  $\hat{p}_{\text{data}}$  is a diffusion with the same diffusion coefficient  $\sqrt{2\tau\beta(s)}$  and state-only drift*

$$\bar{b}_s(X) = \mathbb{E}[b_{s|H}(X) | X_s = X] = -\alpha(s) \sum_i \pi_s(i | X) A_{H^{(i)}}(X) - \beta(s)\gamma(X - M_0),$$

where  $\pi_s(i | X) = p_{s|H^{(i)}}(X) / \sum_j p_{s|H^{(j)}}(X)$ .

*Proof.* Throughout, all densities are with respect to Lebesgue measure on  $\mathbb{R}^{n \times m}$ , and we use  $\nabla \cdot$  and  $\nabla^2$  to denote the divergence and Laplacian operators on  $\mathbb{R}^{n \times m}$  identified with  $\mathbb{R}^{nm}$  via vectorisation. We assume sufficient regularity for the derivatives to be exchanged with the finite sums and conditional expectations below; this holds, in particular, under the smoothness assumptions used elsewhere in the appendix (strictly positive  $C^1$  conditional densities, square-integrable solutions to the forward SDE).

For each  $H \in \mathcal{D}$ , the conditional density  $p_{s|H}$  of the forward SDE (7) satisfies the Fokker–Planck (Kolmogorov forward) equation [17]

$$\partial_s p_{s|H}(X) = -\nabla \cdot (b_{s|H}(X) p_{s|H}(X)) + \tau\beta(s) \nabla^2 p_{s|H}(X), \quad (19)$$

where  $b_{s|H}(X) = -\alpha(s)\mathcal{A}_H(X) - \beta(s)\gamma(X - M_0)$  is the conditional drift in (13) and the diffusion contribution is  $\frac{1}{2}(2\tau\beta(s))\nabla^2 = \tau\beta(s)\nabla^2$  because the diffusion coefficient is state-independent and isotropic.

The marginal density under the empirical data measure is  $\hat{p}_s(X) = \frac{1}{N} \sum_i p_{s|H^{(i)}}(X)$ . Averaging (19) over  $i$  — which is achievable by recognising that the right-hand side is linear in  $p_{s|H}$  for each fixed drift  $b_{s|H}$  — gives

$$\partial_s \hat{p}_s(X) = -\frac{1}{N} \sum_i \nabla \cdot (b_{s|H^{(i)}}(X) p_{s|H^{(i)}}(X)) + \tau\beta(s) \nabla^2 \hat{p}_s(X). \quad (20)$$

The diffusion term is the same as for any individual conditional density because the diffusion coefficient does not depend on  $H$ .

We show that the drift sum in (20) equals  $\nabla \cdot (\bar{b}_s(X) \hat{p}_s(X))$  for the state-only drift  $\bar{b}_s$  of the lemma. Define the posterior weights

$$\pi_s(i | X) := \frac{p_{s|H^{(i)}}(X)}{\sum_j p_{s|H^{(j)}}(X)} = \frac{p_{s|H^{(i)}}(X)}{N \hat{p}_s(X)},$$

so that  $\pi_s(\cdot | X)$  is a probability distribution over  $\{1, \dots, N\}$  for every  $X$  in the support of  $\hat{p}_s$ , and  $p_{s|H^{(i)}}(X) = N \pi_s(i | X) \hat{p}_s(X)$ . Substituting into the drift sum,

$$\frac{1}{N} \sum_i b_{s|H^{(i)}}(X) p_{s|H^{(i)}}(X) = \frac{1}{N} \sum_i b_{s|H^{(i)}}(X) \cdot N \pi_s(i | X) \hat{p}_s(X) \quad (21)$$

$$= \hat{p}_s(X) \sum_i \pi_s(i | X) b_{s|H^{(i)}}(X). \quad (22)$$

Defining

$$\bar{b}_s(X) := \sum_i \pi_s(i | X) b_{s|H^{(i)}}(X) = \mathbb{E}_{\hat{p}_{\text{data}}}[b_{s|H}(X) | X_s = X], \quad (23)$$

the drift sum equals  $\bar{b}_s(X) \hat{p}_s(X)$ , and (20) becomes

$$\partial_s \hat{p}_s(X) = -\nabla \cdot (\bar{b}_s(X) \hat{p}_s(X)) + \tau \beta(s) \nabla^2 \hat{p}_s(X). \quad (24)$$

The second equality in (23) follows from the Bayes-rule identity for the posterior over the latent index  $I$  given  $X_s = X$  under the empirical data measure:  $(H, X_s) = (H^{(I)}, X_s)$  with  $I \sim \text{Uniform}\{1, \dots, N\}$  and  $X_s | I = i \sim p_{s|H^{(i)}}$ , so  $\Pr(I = i | X_s = X) = \pi_s(i | X)$ .

Equation (24) is the Fokker–Planck equation of the SDE

$$dX_s = \bar{b}_s(X_s) ds + \sqrt{2\tau\beta(s)} dW_s,$$

which has state-independent diffusion coefficient  $\sqrt{2\tau\beta(s)}$  and state-only drift  $\bar{b}_s$ . Substituting the explicit form  $b_{s|H}(X) = -\alpha(s)\mathcal{A}_H(X) - \beta(s)\gamma(X - M_0)$  into (23) and using that the OU term is  $H$ -independent,

$$\bar{b}_s(X) = -\alpha(s) \sum_i \pi_s(i | X) \mathcal{A}_{H^{(i)}}(X) - \beta(s)\gamma(X - M_0),$$

which gives the expression in the statement of the lemma.  $\square$

*Remark A.4.* The marginalisation identity used here – that a finite mixture of diffusions sharing a common state-independent diffusion coefficient is itself a diffusion with drift equal to the conditional expectation of the per-component drifts given the current state – is standard. The elementary derivation appears in Brigo [6] for the finite-mixture case (Proposition 1.2 and Corollary 1.3), and the same identity is implicit in standard score-based diffusion derivations (e.g. Song et al. [38]). The subsequent application of Anderson’s time-reversal formula to the marginal diffusion is justified under finite-entropy conditions by the recent low-regularity time-reversal results of Cattiaux et al. [8].

**Theorem A.5** (Conditional reverse drift and  $L^2$ -optimal state-only regression). *Fix  $\mathcal{D} = \{H^{(1)}, \dots, H^{(N)}\} \subset \{0, 1\}^{n \times m}$  and let  $\hat{p}_{\text{data}} = \frac{1}{N} \sum_i \delta_{H^{(i)}}$ . Fix  $s \in (0, S]$ , and for each  $H \in \mathcal{D}$  let  $b_{s|H}(X) = -\alpha(s)\mathcal{A}_H(X) - \beta(s)\gamma(X - M_0)$ . Assume the conditional laws  $p_{s|H^{(i)}}$  are strictly positive  $C^1$  densities. Then:*

(i) *the conditional reverse-time drift is  $u_{s|H}^*(X) = -b_{s|H}(X) + 2\tau\beta(s)r_{s|H}^*(X) = \alpha(s)\mathcal{A}_H(X) + \beta(s)\gamma(X - M_0) + 2\tau\beta(s)r_{s|H}^*(X)$ ;*

(ii) *whenever  $C_s(H) \succ 0$ ,  $r_{s|H}^*(X) = -\text{mat}(C_s(H)^{-1}(\text{vec}(X) - m_s(H)))$ ;*

(iii) *the posterior-averaged reverse drift  $\bar{u}_s^*(X) := \sum_i \pi_s(i | X) u_{s|H^{(i)}}^*(X)$  satisfies*

$$\bar{u}_s^*(X) = \alpha(s) \sum_i \pi_s(i | X) \mathcal{A}_{H^{(i)}}(X) + \beta(s)\gamma(X - M_0) + 2\tau\beta(s)\nabla_X \log \hat{p}_s(X);$$

(iv) *the  $L^2$ -optimal state-only predictor for the population objective (15) is  $u_s^{L^2}(X) = \bar{u}_s^*(X)$ .*

*Moreover, the state-only marginal reverse drift of the forward process coincides with this predictor: by Lemma A.3 and the Anderson/Haussmann–Pardoux time-reversal formula [2; 20], the marginal reverse SDE has state-only drift  $u_s^*(X) = -\bar{b}_s(X) + 2\tau\beta(s)\nabla_X \log \hat{p}_s(X) = \bar{u}_s^*(X)$ .*

*Proof.* (i) For state-independent diffusion coefficient  $\sigma_s = \sqrt{2\tau\beta(s)}$ , the general Anderson–Haussmann–Pardoux time-reversal formula  $u_{s|H}^*(X) = -b_{s|H}(X) + \nabla_X \cdot (p_{s|H}(X) \sigma_s \sigma_s^\top) / p_{s|H}(X)$  [2; 20] simplifies to

$$u_{s|H}^*(X) = -b_{s|H}(X) + \sigma_s^2 \nabla_X \log p_{s|H}(X),$$

because  $\sigma_s$  does not depend on the state and so the divergence term collapses to  $\sigma_s^2 \nabla_X p_{s|H} / p_{s|H} = \sigma_s^2 \nabla_X \log p_{s|H}$ . Substituting the explicit form of  $b_{s|H}$  from (13) gives

$$u_{s|H}^*(X) = \alpha(s) \mathcal{A}_H(X) + \beta(s) \gamma(X - M_0) + 2\tau\beta(s) r_{s|H}^*(X).$$

(ii) Direct from  $\nabla_x \log \mathcal{N}(x; m, C) = -C^{-1}(x - m)$  applied to the vectorised conditional law  $\text{vec}(X_s) | H \sim \mathcal{N}(m_s(H), C_s(H))$  established in Proposition 3.2, then reshaped to matrix form via  $\text{mat}$ . Invertibility of  $C_s(H)$  for  $s \in (0, S]$  also follows from Proposition 3.2.

(iii) Expand  $\bar{u}_s^*$  using (i):

$$\bar{u}_s^*(X) = \alpha(s) \sum_i \pi_s(i | X) A_{H^{(i)}}(X) + \beta(s) \gamma(X - M_0) + 2\tau\beta(s) \sum_i \pi_s(i | X) r_{s|H^{(i)}}^*(X).$$

The structural term is the posterior-weighted sum, the OU term is  $H$ -independent (and so its average over  $\pi_s(\cdot | X)$  is unchanged), and the score term is handled by the mixture-score identity

$$\begin{aligned} \sum_i \pi_s(i | X) r_{s|H^{(i)}}^*(X) &= \sum_i \frac{p_{s|H^{(i)}}(X)}{\sum_j p_{s|H^{(j)}}(X)} \frac{\nabla_X p_{s|H^{(i)}}(X)}{p_{s|H^{(i)}}(X)} \\ &= \frac{\sum_i \nabla_X p_{s|H^{(i)}}(X)}{\sum_j p_{s|H^{(j)}}(X)} = \frac{\frac{1}{N} \sum_i \nabla_X p_{s|H^{(i)}}(X)}{\frac{1}{N} \sum_j p_{s|H^{(j)}}(X)} \\ &= \frac{\nabla_X \hat{p}_s(X)}{\hat{p}_s(X)} = \nabla_X \log \hat{p}_s(X), \end{aligned}$$

where the third equality multiplies numerator and denominator by  $1/N$  and the fourth uses linearity of  $\nabla_X$  together with  $\hat{p}_s(X) = \frac{1}{N} \sum_i p_{s|H^{(i)}}(X)$ .

(iv) Conditioning on  $X_s$ , the population objective (15) decomposes by the Tower property as

$$\mathcal{L}(\theta) = \mathbb{E}_{s \sim \rho} \mathbb{E}_{X_s \sim \hat{p}_s} \left[ \mathbb{E}[\|u_s^\theta(X_s) - u_{s|H}^*(X_s)\|_F^2 | X_s] \right].$$

For each  $X$ , the inner conditional expectation is minimised pointwise over  $u_s^\theta(X) \in \mathbb{R}^{n \times m}$  by the conditional expectation  $\mathbb{E}[u_{s|H}^*(X_s) | X_s = X]$ , since  $L^2$ -projection onto the  $\sigma(X_s)$ -measurable random variables coincides with conditional expectation [5, Sec. 34]. Under the empirical data measure, the joint law of  $(H, X_s)$  is obtained by sampling  $I \sim \text{Uniform}\{1, \dots, N\}$  and  $X_s \sim p_{s|H^{(I)}}$ , and the posterior law of  $I$  given  $X_s = X$  is  $\text{Pr}(I = i | X_s = X) = \pi_s(i | X)$  by Bayes' rule. Hence

$$u_s^{L^2}(X) = \mathbb{E}[u_{s|H}^*(X_s) | X_s = X] = \sum_i \pi_s(i | X) u_{s|H^{(i)}}^*(X) = \bar{u}_s^*(X),$$

where the last equality is the definition of  $\bar{u}_s^*$  in (iii).

By Lemma A.3, the marginal forward process under  $\hat{p}_{\text{data}}$  is a diffusion with state-independent diffusion coefficient  $\sigma_s = \sqrt{2\tau\beta(s)}$  and state-only drift  $\bar{b}_s$ . The marginal density  $\hat{p}_s(X) = \frac{1}{N} \sum_i p_{s|H^{(i)}}(X)$  is a finite uniform average of strictly positive  $C^1$  densities, hence itself strictly positive and  $C^1$ , so the regularity hypotheses of Haussmann and Pardoux [20] are satisfied for the marginal diffusion. Applying the same simplification as in (i) (the divergence term collapses because  $\sigma_s$  is state-independent), the marginal reverse SDE has state-only drift

$$u_s^*(X) = -\bar{b}_s(X) + \sigma_s^2 \nabla_X \log \hat{p}_s(X).$$

Substituting  $\bar{b}_s(X) = -\alpha(s) \sum_i \pi_s(i | X) A_{H^{(i)}}(X) - \beta(s) \gamma(X - M_0)$  from Lemma A.3 matches the expression for  $\bar{u}_s^*(X)$  given in (iii) term-by-term, so  $u_s^* = \bar{u}_s^* = u_s^{L^2}$ .  $\square$

**Proposition A.6** (Exactness under a state-only reverse representation). *Let  $\{\hat{p}_s\}_{s \in [0, S]}$  be the marginal forward family under  $\hat{p}_{\text{data}}$ , with  $\hat{p}_0 = \hat{p}_{\text{data}}$  and  $\hat{p}_S$  the terminal law under (7). If the reverse SDE  $dY_t = \bar{u}_{S-t}^*(Y_t) dt + \sqrt{2\tau\beta(S-t)} d\bar{W}_t$  is well-posed and initialised from  $Y_0 \sim \hat{p}_S$ , and if it is solved exactly, then  $\text{Law}(Y_t) = \hat{p}_{S-t}$  for all  $t$ , and in particular  $\text{Law}(Y_S) = \hat{p}_{\text{data}}$ .*

*Proof.* By Lemma A.3, the marginal forward process under  $\hat{p}_{\text{data}}$  is a diffusion with state-independent diffusion coefficient  $\sigma_s := \sqrt{2\tau\beta(s)}$  and state-only drift  $\bar{b}_s$ . Its marginal density  $\hat{p}_s$  therefore satisfies the forward Fokker–Planck equation

$$\partial_s \hat{p}_s(X) = -\nabla_X \cdot (\bar{b}_s(X) \hat{p}_s(X)) + \tau\beta(s) \nabla_X^2 \hat{p}_s(X), \quad s \in [0, S], \quad (25)$$

with initial condition  $\hat{p}_0 = \hat{p}_{\text{data}}$  and terminal density  $\hat{p}_S$ . Since  $\hat{p}_s$  is a finite uniform average of the strictly positive  $C^1$  conditional densities  $p_{s|H^{(i)}}$  for each  $s \in (0, S]$ ,  $\hat{p}_s$  is itself strictly positive and  $C^1$  on  $(0, S]$ , so the regularity hypotheses of the time-reversal theorem below are satisfied.

By the Haussmann–Pardoux time-reversal theorem [20] applied to the marginal forward diffusion, there exists a reverse-time process  $Z_\bullet$  on  $[0, S]$ , defined on a common stochastic basis, such that  $Z_t \stackrel{d}{=} X_{S-t}$  for all  $t \in [0, S]$ , satisfying

$$dZ_t = u_{S-t}^*(Z_t) dt + \sigma_{S-t} d\bar{W}_t, \quad Z_0 \sim \hat{p}_S, \quad (26)$$

with state-only drift

$$u_s^*(X) := -\bar{b}_s(X) + \sigma_s^2 \nabla_X \log \hat{p}_s(X). \quad (27)$$

Equivalently, writing the Fokker–Planck equation of  $Z_t$  in reverse time (i.e. for the family  $q_t := \hat{p}_{S-t}$ , so that  $\partial_t q_t = -\partial_s \hat{p}_s|_{s=S-t}$ ), one verifies by direct substitution into (25) that  $q_t$  satisfies

$$\partial_t q_t(X) = -\nabla_X \cdot (u_{S-t}^*(X) q_t(X)) + \tau\beta(S-t) \nabla_X^2 q_t(X), \quad q_0 = \hat{p}_S,$$

which is exactly the forward Fokker–Planck equation of the SDE (26). Since  $\hat{p}_s$  is a strictly positive  $C^1$  density on  $(0, S]$ , this reverse Fokker–Planck equation has the unique solution  $q_t = \hat{p}_{S-t}$ .

By Theorem A.5, the marginal reverse drift  $u_s^*$  defined in (27) coincides termwise with the posterior-averaged reverse drift  $\bar{u}_s^*$ :

$$u_s^*(X) = \bar{u}_s^*(X) = \alpha(s) \sum_i \pi_s(i | X) A_{H^{(i)}}(X) + \beta(s)\gamma(X - M_0) + 2\tau\beta(s) \nabla_X \log \hat{p}_s(X).$$

Hence the SDE (26) with drift  $u_s^*$  is the same SDE as the one in the proposition statement with drift  $\bar{u}_s^*$ , and they have the same family of laws.

Combining these steps together: if  $Y_t$  solves  $dY_t = \bar{u}_{S-t}^*(Y_t) dt + \sigma_{S-t} d\bar{W}_t$  exactly, with  $Y_0 \sim \hat{p}_S$ , then  $Y_\bullet$  has the same law as  $Z_\bullet$  in (26) (same drift, same diffusion coefficient, same initial law). Consequently  $\text{Law}(Y_t) = \text{Law}(Z_t) = \hat{p}_{S-t}$  for all  $t \in [0, S]$  and by weak continuity of the diffusion at the endpoint,  $\text{Law}(Y_s)$  is the weak limit  $\lim_{s \downarrow 0} \hat{p}_s = \hat{p}_{\text{data}}$ .  $\square$

In practice, HEDGE initialises generation from  $\mathcal{N}(M_0, (\tau/\gamma)I)$  rather than  $\hat{p}_S$ . The discrepancy  $\nu_0^\theta \neq \nu_0^* := \hat{p}_S$ , together with the training error and solver error, is controlled by the finite-horizon stability results below. More elaborate initialisation schemes, for example learned Gaussianising transports of the kind used in transport-based Monte Carlo [16; 7], could also be analysed through the same initialisation term, but we leave such refinements to future work.

#### A.4 Stability via a one-sided Lipschitz $W_2$ bound

**Definition A.7** (One-sided Lipschitz constant). A measurable function  $\kappa : [0, S] \rightarrow \mathbb{R}$  is a one-sided Lipschitz constant of  $v : [0, S] \times \mathbb{R}^{n \times m} \rightarrow \mathbb{R}^{n \times m}$  if  $\langle X - Y, v_s(X) - v_s(Y) \rangle_F \leq \kappa_s \|X - Y\|_F^2$  for all  $X, Y, s$ .

**Theorem A.8** ( $W_2$  stability via one-sided Lipschitz). Let  $u_s^*, u_s^\theta$  be measurable time-dependent drift fields on  $[0, S]$ , and consider the reverse-time SDEs

$$dY_t^* = u_{S-t}^*(Y_t^*) dt + \sqrt{2\tau\beta(S-t)} d\bar{W}_t, \quad Y_0^* \sim \nu_0^*, \quad (28)$$

$$dY_t^\theta = u_{S-t}^\theta(Y_t^\theta) dt + \sqrt{2\tau\beta(S-t)} d\bar{W}_t, \quad Y_0^\theta \sim \nu_0^\theta, \quad (29)$$

driven by the same Brownian motion. Assume both are well-posed with square-integrable solutions, and that  $u^\theta$  has a one-sided Lipschitz constant  $\kappa : [0, S] \rightarrow \mathbb{R}$ . Define the error as  $e_t := u_{S-t}^\theta(Y_t^*) - u_{S-t}^*(Y_t^*)$  and let  $\Lambda(t) := \int_0^t (2\kappa_{S-r} + 1) dr$ . Then

$$\mathbb{E} \|Y_t^\theta - Y_t^*\|_F^2 \leq e^{\Lambda(t)} \left( \mathbb{E} \|Y_0^\theta - Y_0^*\|_F^2 + \int_0^t e^{-\Lambda(r)} \mathbb{E} \|e_r\|_F^2 dr \right), \quad (30)$$

and consequently

$$W_2(\text{Law}(Y_t^\theta), \text{Law}(Y_t^*)) \leq e^{\Lambda(t)/2} \left( W_2(\nu_0^\theta, \nu_0^*)^2 + \int_0^t e^{-\Lambda(r)} \mathbb{E} \|e_r\|_F^2 dr \right)^{1/2}. \quad (31)$$

If  $\kappa_s \leq L$  uniformly (global Lipschitz),  $\Lambda(t) \leq (2L+1)t$  recovers the standard Grönwall estimate. If  $\kappa_s \leq \kappa_* < -1/2$  uniformly, then  $e^{\Lambda(S)/2} < 1$ .

*Proof.* Let  $\Delta_t := Y_t^\theta - Y_t^*$ . Since both SDEs share the same Brownian motion and diffusion coefficient, the stochastic terms cancel:  $d\Delta_t = [u_{S-t}^\theta(Y_t^\theta) - u_{S-t}^*(Y_t^*)] dt$ .

By adding and subtracting  $u_{S-t}^\theta(Y_t^*)$  we have,

$$d\Delta_t = a_t dt + e_t dt, \quad a_t := u_{S-t}^\theta(Y_t^\theta) - u_{S-t}^\theta(Y_t^*).$$

$\Delta_t$  has absolutely continuous paths, and for a.e.  $t$ , then by the chain rule  $\frac{d}{dt} \|\Delta_t\|_F^2 = 2\langle \Delta_t, a_t \rangle_F + 2\langle \Delta_t, e_t \rangle_F$ .

By the one-sided Lipschitz definition (Definition A.7),  $2\langle \Delta_t, a_t \rangle_F \leq 2\kappa_{S-t} \|\Delta_t\|_F^2$ . By Young's inequality,  $2\langle \Delta_t, e_t \rangle_F \leq \|\Delta_t\|_F^2 + \|e_t\|_F^2$ . Hence

$$\frac{d}{dt} \|\Delta_t\|_F^2 \leq (2\kappa_{S-t} + 1) \|\Delta_t\|_F^2 + \|e_t\|_F^2.$$

Taking expectations of both sides of the pathwise inequality and using Fubini's theorem to interchange the time derivative with the expectation (justified by square-integrability of the solutions),

$$\frac{d}{dt} \mathbb{E} \|\Delta_t\|_F^2 \leq (2\kappa_{S-t} + 1) \mathbb{E} \|\Delta_t\|_F^2 + \mathbb{E} \|e_t\|_F^2.$$

Define the shorthand

$$f(t) := \mathbb{E} \|\Delta_t\|_F^2, \quad g(t) := \mathbb{E} \|e_t\|_F^2, \quad \mu(t) := 2\kappa_{S-t} + 1, \quad \Lambda(t) := \int_0^t \mu(r) dr,$$

so the inequality becomes  $f'(t) \leq \mu(t) f(t) + g(t)$ . Applying the standard integrating-factor identity for linear differential inequalities, multiplying both sides by  $e^{-\Lambda(t)}$  and using  $\Lambda'(t) = \mu(t)$ ,

$$\frac{d}{dt} \left( e^{-\Lambda(t)} f(t) \right) = e^{-\Lambda(t)} (f'(t) - \mu(t) f(t)) \leq e^{-\Lambda(t)} g(t).$$

Integrating this inequality from 0 to  $t$ , and using  $\Lambda(0) = 0$ ,

$$e^{-\Lambda(t)} f(t) - f(0) \leq \int_0^t e^{-\Lambda(r)} g(r) dr.$$

Multiplying through by  $e^{\Lambda(t)}$  and substituting back the definitions of  $f$  and  $g$  gives the mean-square bound (30).

The coupling  $(Y_0^\theta, Y_0^*)$  at  $t = 0$  can be chosen as the optimal  $W_2$ -coupling of  $(\nu_0^\theta, \nu_0^*)$ , so that  $\mathbb{E} \|Y_0^\theta - Y_0^*\|_F^2 = W_2(\nu_0^\theta, \nu_0^*)^2$ . The synchronously-coupled processes  $(Y_t^\theta, Y_t^*)$  obtained by solving (28)–(29) under the same Brownian motion then form a (not-necessarily-optimal) coupling of  $(\text{Law}(Y_t^\theta), \text{Law}(Y_t^*))$  at every later  $t \in (0, S]$ , hence by the definition of  $W_2$  as an infimum over couplings,

$$W_2(\text{Law}(Y_t^\theta), \text{Law}(Y_t^*))^2 \leq \mathbb{E} \|Y_t^\theta - Y_t^*\|_F^2 = f(t).$$

Substituting (30) and taking square roots yields the  $W_2$  bound (31).  $\square$

*Remark A.9* (Why the one-sided constant improves on Lipschitz in the HEDGE setting). For the exact target  $u_s^*(X) = \alpha(s)\bar{A}_s(X) + \beta(s)\gamma(X - M_0) + 2\tau\beta(s)\nabla_X \log \hat{p}_s(X)$ , where  $\bar{A}_s(X) := \sum_i \pi_s(i | X) \mathcal{A}_{H^{(i)}}(X)$ , the linear-in- $X$  part of the heat term is PSD, so contributes 0 to  $\kappa_s$  from above; the OU term contributes exactly  $-\beta(s)\gamma$ ; only the score Jacobian contributes positively. Hence  $\kappa_s \leq -\beta(s)\gamma + 2\tau\beta(s)L_s^{\text{score}}$ , where  $L_s^{\text{score}}$  is a one-sided Lipschitz bound on  $\nabla_X \log \hat{p}_s$ . Since  $\hat{p}_s$  is a smooth Gaussian mixture for  $s \in (0, S]$ ,  $L_s^{\text{score}}$  is finite on any subinterval bounded away from  $s = 0$  (it may diverge as  $s \downarrow 0$  because  $\hat{p}_0 = \hat{p}_{\text{data}}$  is supported on a finite set). Whenever  $2\tau L_s^{\text{score}} < \gamma$  uniformly on the operating interval,  $\kappa_s < 0$  there, and the corresponding contribution to  $e^{\Lambda(S)/2}$  is contractive. The conclusion of Theorem A.8, which requires the one-sided Lipschitz bound on  $u^*$ , applies whenever the score Jacobian satisfies this ground condition.

### A.5 Euler–Maruyama discretisation error

**Corollary A.10** (Euler–Maruyama numerical error). *Assume  $u_s^\theta$  is globally Lipschitz in state uniformly in  $s$ , has at most linear growth, and is continuous in  $s$  uniformly on bounded state sets; and assume  $\sqrt{\beta}$  is bounded and Lipschitz on  $[0, S]$ . Let  $0 = t_0 < t_1 < \dots < t_K = S$  be a uniform grid with  $\Delta t = S/K$ , and let  $\hat{Y}^\theta$  be the Euler–Maruyama approximation of the learned reverse SDE (29). Then there is  $C > 0$ , independent of  $\Delta t$ , such that*

$$\mathbb{E}\|Y_S^\theta - \hat{Y}_S^\theta\|_F^2 \leq C \Delta t, \quad W_2(\text{Law}(Y_S^\theta), \text{Law}(\hat{Y}_S^\theta)) \leq C^{1/2} \Delta t^{1/2}.$$

*Proof. Vectorisation.* The map  $\text{vec} : \mathbb{R}^{n \times m} \rightarrow \mathbb{R}^{nm}$  is a linear isometry,  $\|\text{vec}(X)\|_2 = \|X\|_F$  for all  $X \in \mathbb{R}^{n \times m}$ . Vectorising the learned reverse SDE (29) gives the equivalent vector SDE on  $\mathbb{R}^{nm}$ ,

$$dy_t = \tilde{u}_{S-t}^\theta(y_t) dt + \sqrt{2\tau\beta(S-t)} d\bar{w}_t, \quad y_0 \sim \text{vec}(v_0^\theta),$$

where  $\tilde{u}_s^\theta(y) := \text{vec}(u_s^\theta(\text{mat}(y)))$  and  $\bar{w}_t = \text{vec}(\bar{W}_t)$  is a standard  $nm$ -dimensional Brownian motion. The assumptions on  $u^\theta$  transfer to  $\tilde{u}^\theta$  without change: the global state-Lipschitz, linear-growth, and  $s$ -continuity properties are preserved by composition with the isometry. The diffusion coefficient  $\sqrt{2\tau\beta(S-t)}$  is deterministic, independent of state, and Lipschitz in  $t$  by the assumed Lipschitz regularity of  $\beta$ , so the standard regularity on the diffusion coefficient (state-Lipschitz, linear growth) are automatically satisfied.

*Strong-order-1/2 Euler–Maruyama bound.* Under these assumptions, the standard Euler–Maruyama convergence theorem for SDEs with state-Lipschitz linear-growth drift and time-Lipschitz state-independent diffusion coefficient [25, Ch. 10] [21, Sec. 4] gives the strong-order-1/2 bound

$$\mathbb{E}\|y_S - \hat{y}_S\|_2^2 \leq C \Delta t,$$

where  $\hat{y}_S$  is the Euler–Maruyama approximation on the same probability space as  $y_S$ , and  $C > 0$  depends on the Lipschitz and linear-growth constants of  $\tilde{u}^\theta$ , on  $\sup_{s \in [0, S]} \beta(s)$ , on the Lipschitz constant of  $\beta$ , and on  $S$ , but not on  $\Delta t$ .

*Transport back to matrix form.* Reshaping  $y_S = \text{vec}(Y_S^\theta)$  and  $\hat{y}_S = \text{vec}(\hat{Y}_S^\theta)$  via the inverse isometry  $\text{mat}$ , and using  $\|\text{vec}(X)\|_2 = \|X\|_F$ ,

$$\mathbb{E}\|Y_S^\theta - \hat{Y}_S^\theta\|_F^2 = \mathbb{E}\|y_S - \hat{y}_S\|_2^2 \leq C \Delta t.$$

For the  $W_2$  bound, the pair  $(Y_S^\theta, \hat{Y}_S^\theta)$  is a coupling of  $(\text{Law}(Y_S^\theta), \text{Law}(\hat{Y}_S^\theta))$  since both are defined on the same probability space, so by the definition of  $W_2$  [10],

$$W_2(\text{Law}(Y_S^\theta), \text{Law}(\hat{Y}_S^\theta))^2 \leq \mathbb{E}\|Y_S^\theta - \hat{Y}_S^\theta\|_F^2 \leq C \Delta t,$$

and taking square roots gives the result.  $\square$

### A.6 Total generation-error decomposition

**Corollary A.11** (Total generation error). *Under the assumptions of Proposition A.6, Theorem A.8, and Corollary A.10,*

$$W_2(\text{Law}(\hat{Y}_S^\theta), \hat{p}_{\text{data}}) \leq C^{1/2} \Delta t^{1/2} + e^{\Lambda(S)/2} \mathcal{E}_{\text{rev}}, \quad (32)$$

where  $\Lambda(S) = \int_0^S (2\kappa_{S-r} + 1) dr$  as in Theorem A.8, and

$$\mathcal{E}_{\text{rev}}^2 := W_2(v_0^\theta, v_0^*)^2 + \int_0^S e^{-\Lambda(r)} \mathbb{E}\|u_{S-r}^\theta(Y_r^\theta) - u_{S-r}^*(Y_r^\theta)\|_F^2 dr.$$

*In the ideal case  $u^\theta = u^*$  with exact initialisation  $v_0^\theta = v_0^*$ , the second term vanishes and only the  $O(\Delta t^{1/2})$  Euler–Maruyama term remains.*

*Proof.* The proof follows from the triangle-inequality decomposition of the total error into a stability contribution and a discretisation contribution, each of which is controlled by an earlier result.

Under the assumptions of Proposition A.6, the ideal reverse SDE (28) initialised from  $Y_0^* \sim v_0^* = \hat{p}_S$  and solved exactly satisfies  $\text{Law}(Y_S^*) = \hat{p}_{\text{data}}$ .

Inserting the intermediate law  $\text{Law}(Y_S^\theta)$  — the law of the exact solution of the learned reverse SDE at time  $S$  — between the Euler–Maruyama approximation  $\widehat{Y}_S^\theta$  and the data law, and using the triangle inequality for  $W_2$  gives,

$$W_2(\text{Law}(\widehat{Y}_S^\theta), \hat{p}_{\text{data}}) \leq \underbrace{W_2(\text{Law}(\widehat{Y}_S^\theta), \text{Law}(Y_S^\theta))}_{\text{discretisation error}} + \underbrace{W_2(\text{Law}(Y_S^\theta), \text{Law}(Y_S^*))}_{\text{stability error}}.$$

The discretisation error (first right-hand-side term) is bounded by Corollary A.10,

$$W_2(\text{Law}(\widehat{Y}_S^\theta), \text{Law}(Y_S^\theta)) \leq C^{1/2} \Delta t^{1/2}.$$

The stability error (second right-hand-side term) is bounded by Theorem A.8 applied at  $t = S$ ,

$$W_2(\text{Law}(Y_S^\theta), \text{Law}(Y_S^*)) \leq e^{\Lambda(S)/2} \mathcal{E}_{\text{rev}}.$$

Adding the two bounds gives (32).

*Ideal case.* Note that if  $u^\theta = u^*$  pointwise on  $[0, S] \times \mathbb{R}^{n \times m}$ , the drift-error integrand  $\|u_{S-t}^\theta(Y_t^*) - u_{S-t}^*(Y_t^*)\|_F^2$  is zero, and if additionally  $\nu_0^\theta = \nu_0^*$ , then  $W_2(\nu_0^\theta, \nu_0^*) = 0$ . Hence  $\mathcal{E}_{\text{rev}} = 0$ , the stability term in (32) vanishes, and only the  $O(\Delta t^{1/2})$  Euler–Maruyama term remains.  $\square$

### A.7 Equivariance of the $L^2$ -optimal target

Let  $P \in \mathbb{R}^{n \times n}$  and  $Q \in \mathbb{R}^{m \times m}$  be permutation matrices. The action of  $S_n \times S_m$  on incidence-space states is

$$X \mapsto PXQ^\top, \quad X \in \mathbb{R}^{n \times m}.$$

We write  $\mathcal{T}_{P,Q}(X) := PXQ^\top$ . This map is orthogonal with respect to the Frobenius inner product and has unit absolute Jacobian determinant.

**Lemma A.12** (Equivariance of the row- and column-side Laplacians). *For any  $H \in \{0, 1\}^{n \times m}$ ,*

$$L_V(PHQ^\top) = PL_V(H)P^\top, \quad L_E(PHQ^\top) = QL_E(H)Q^\top.$$

*Consequently, for the two-sided heat operator*

$$\mathcal{A}_H(X) := L_V(H)X + XL_E(H),$$

*one has*

$$\mathcal{A}_{PHQ^\top}(PXQ^\top) = P\mathcal{A}_H(X)Q^\top.$$

*Proof.* The node-degree and hyperedge-size diagonal matrices transform as

$$D_V(PHQ^\top) = PD_V(H)P^\top, \quad D_E(PHQ^\top) = QD_E(H)Q^\top.$$

Therefore,

$$\begin{aligned} (PHQ^\top)D_E(PHQ^\top)^{-1}(PHQ^\top)^\top \\ = PHQ^\top(QD_E(H)^{-1}Q^\top)QH^\top P^\top = PHD_E(H)^{-1}H^\top P^\top. \end{aligned}$$

Since diagonal inverse square roots commute with permutation conjugation,

$$D_V(PHQ^\top)^{-1/2} = PD_V(H)^{-1/2}P^\top,$$

which gives  $L_V(PHQ^\top) = PL_V(H)P^\top$ .

For the hyperedge-side operator,

$$(PHQ^\top)^\top(PHQ^\top) = QH^\top H Q^\top,$$

and the same permutation-conjugation identity applies to  $D_E^{-1/2}$ . Moreover,  $\text{offdiag}(\cdot)$  commutes with conjugation by a permutation matrix. Hence

$$A_E(PHQ^\top) = QA_E(H)Q^\top.$$

It follows that

$$D_{\text{ov}}(PHQ^\top) = QD_{\text{ov}}(H)Q^\top,$$

and therefore

$$L_E(PHQ^\top) = QL_E(H)Q^\top.$$

The final claim follows by direct substitution:

$$\begin{aligned} \mathcal{A}_{PHQ^\top}(PXQ^\top) &= PL_V(H)P^\top PXQ^\top + PXQ^\top QL_E(H)Q^\top \\ &= P(L_V(H)X + XL_E(H))Q^\top = P\mathcal{A}_H(X)Q^\top. \end{aligned}$$

$\square$

**Lemma A.13** (Equivariance of the conditional forward and reverse laws). *Assume  $PM_0Q^\top = M_0$ , and let the matrix Brownian motion be isotropic, so that*

$$PW_sQ^\top \stackrel{d}{=} W_s.$$

Let  $X_s^H$  denote the solution of the forward SDE initialised at  $X_0 = H$ . Then

$$X_s^{PHQ^\top} \stackrel{d}{=} PX_s^H Q^\top.$$

Consequently, for every  $s > 0$ ,

$$p_{s|PHQ^\top}(PXQ^\top) = p_{s|H}(X),$$

and the conditional score and conditional reverse drift satisfy

$$r_{s|PHQ^\top}^*(PXQ^\top) = Pr_{s|H}^*(X)Q^\top,$$

and

$$u_{s|PHQ^\top}^*(PXQ^\top) = Pu_{s|H}^*(X)Q^\top.$$

*Proof.* Define  $Y_s := PX_s^H Q^\top$ . Since  $P$  and  $Q$  are constant matrices,

$$dY_s = P dX_s^H Q^\top.$$

Substituting the forward SDE gives

$$dY_s = -\alpha(s)PA_H(X_s^H)Q^\top ds - \beta(s)\gamma P(X_s^H - M_0)Q^\top ds + \sqrt{2\tau\beta(s)} P dW_s Q^\top.$$

By Lemma A.12,

$$PA_H(X_s^H)Q^\top = \mathcal{A}_{PHQ^\top}(PX_s^H Q^\top) = \mathcal{A}_{PHQ^\top}(Y_s),$$

and by the assumed invariance of  $M_0$ ,

$$P(X_s^H - M_0)Q^\top = Y_s - M_0.$$

Finally, isotropy of the Brownian motion gives

$$P dW_s Q^\top \stackrel{d}{=} dW_s.$$

Thus  $Y_s$  satisfies the same SDE in law as the process initialised at  $PHQ^\top$ . Since  $Y_0 = PHQ^\top$ , uniqueness in law yields

$$X_s^{PHQ^\top} \stackrel{d}{=} PX_s^H Q^\top.$$

Because  $\mathcal{T}_{P,Q}$  is an orthogonal transformation with unit absolute Jacobian determinant, the density identity follows:

$$p_{s|PHQ^\top}(PXQ^\top) = p_{s|H}(X).$$

Differentiating with respect to  $X$  under the orthogonal change of variables gives the score transformation

$$r_{s|PHQ^\top}^*(PXQ^\top) = Pr_{s|H}^*(X)Q^\top.$$

The conditional reverse drift is

$$u_{s|H}^*(X) = \alpha(s)\mathcal{A}_H(X) + \beta(s)\gamma(X - M_0) + 2\tau\beta(s)r_{s|H}^*(X).$$

Combining the equivariance of  $\mathcal{A}_H$ , the invariance of  $M_0$ , and the score transformation gives

$$u_{s|PHQ^\top}^*(PXQ^\top) = Pu_{s|H}^*(X)Q^\top.$$

□

**Theorem A.14** (Equivariance of the  $L^2$ -optimal reverse-drift target). *Assume that the empirical data measure  $\hat{p}_{\text{data}}$  is invariant under the action  $H \mapsto PHQ^\top$ , that  $PM_0Q^\top = M_0$ , and that the driving Brownian motion is isotropic. Let*

$$\hat{p}_s(X) := \int p_{s|H}(X) \hat{p}_{\text{data}}(dH)$$

be the marginal forward density induced by the empirical data measure, and let

$$u_s^{L^2}(X) := \mathbb{E}_{\hat{p}_{\text{data}}} \left[ u_{s|H}^*(X) \mid X_s = X \right]$$

be the  $L^2$ -optimal state-only reverse-drift target. Then

$$\hat{p}_s(PXQ^\top) = \hat{p}_s(X)$$

and

$$u_s^{L^2}(PXQ^\top) = Pu_s^{L^2}(X)Q^\top.$$

*Proof.* First consider the marginal density. Using Lemma A.13,

$$p_{s|H}(PXQ^\top) = p_{s|P^\top HQ}(X).$$

Therefore,

$$\begin{aligned} \hat{p}_s(PXQ^\top) &= \int p_{s|H}(PXQ^\top) \hat{p}_{\text{data}}(dH) \\ &= \int p_{s|P^\top HQ}(X) \hat{p}_{\text{data}}(dH). \end{aligned}$$

By invariance of  $\hat{p}_{\text{data}}$  under  $H \mapsto P^\top HQ$ , the last integral equals

$$\int p_{s|H}(X) \hat{p}_{\text{data}}(dH) = \hat{p}_s(X).$$

We now prove the equivariance of the posterior-averaged reverse drift. Define the posterior measure over the latent training hypergraph by

$$\pi_s(dH | X) := \frac{p_{s|H}(X) \hat{p}_{\text{data}}(dH)}{\hat{p}_s(X)}.$$

Then

$$u_s^{L^2}(X) = \int u_{s|H}^*(X) \pi_s(dH | X).$$

At the transformed state  $PXQ^\top$ ,

$$u_s^{L^2}(PXQ^\top) = \int u_{s|H}^*(PXQ^\top) \frac{p_{s|H}(PXQ^\top)}{\hat{p}_s(PXQ^\top)} \hat{p}_{\text{data}}(dH).$$

Using Lemma A.13 with  $\tilde{H} = P^\top HQ$ , we have

$$u_{s|H}^*(PXQ^\top) = P u_{s|P^\top HQ}^*(X) Q^\top,$$

and

$$p_{s|H}(PXQ^\top) = p_{s|P^\top HQ}(X).$$

Together with  $\hat{p}_s(PXQ^\top) = \hat{p}_s(X)$ , this gives

$$u_s^{L^2}(PXQ^\top) = P \left[ \int u_{s|P^\top HQ}^*(X) \frac{p_{s|P^\top HQ}(X)}{\hat{p}_s(X)} \hat{p}_{\text{data}}(dH) \right] Q^\top.$$

Finally, by invariance of  $\hat{p}_{\text{data}}$ , the change of variable  $\tilde{H} = P^\top HQ$  leaves the empirical measure unchanged, so

$$\begin{aligned} u_s^{L^2}(PXQ^\top) &= P \left[ \int u_{s|\tilde{H}}^*(X) \frac{p_{s|\tilde{H}}(X)}{\hat{p}_s(X)} \hat{p}_{\text{data}}(d\tilde{H}) \right] Q^\top \\ &= P u_s^{L^2}(X) Q^\top. \end{aligned}$$

This proves the claim.  $\square$

## B Additional Numerical Results

### B.1 Real-data benchmarks

We evaluate HEDGE on real hypergraph datasets drawn primarily from the DHG-Bench/AllSet benchmark family [26; 11], together with congressional committee hypergraph data. These datasets were originally introduced for hypergraph learning tasks, especially node classification and hyperedge prediction [45; 34; 37], but in this paper we use only their incidence structure. Node features, labels, and task-specific train/validation/test splits are not used by HEDGE.

A central difficulty in the real-data setting is that each benchmark provides essentially a *single large observed hypergraph*, rather than a collection of many hypergraphs that could be used directly for generative training and evaluation. We therefore construct the learning problem by sampling fixed-size subhypergraphs from this single observed hypergraph. These sampled subhypergraphs provide the train/test objects used by the generative benchmark.

Table 2: Summary statistics of the real hypergraph datasets used in the paper. The statistics describe the full benchmark hypergraphs before fixed-size subhypergraph sampling. Features and classes are part of the original learning benchmarks but are not used by HEDGE.

Dataset	Source family	Nodes $n$	Hyperedges $m$	Avg. edge size $\bar{d}_E$	Avg. node degree $\bar{d}_V$	Density $\rho$	Features	Classes
Cora	Cocitation	2,708	1,579	3.03	1.77	$1.12 \times 10^{-3}$	1,433	7
CiteSeer	Cocitation	3,312	1,079	3.20	1.04	$9.66 \times 10^{-4}$	3,703	6
DBLP	Coauthorship	41,302	22,363	4.45	2.41	$1.08 \times 10^{-4}$	1,425	6
House-Committees	Congressional committees	1,290	340	34.73	9.18	$2.69 \times 10^{-2}$	100	2
Actor	Heterogeneous	16,255	10,164	5.43	3.40	$3.34 \times 10^{-4}$	50	3
Twitch	Heterogeneous	16,812	2,627	6.23	0.97	$3.71 \times 10^{-4}$	7	2

Related divide-and-conquer ideas appear, for example, in scalable Monte Carlo methods, where data are partitioned, subposterior simulations are run independently, and the resulting samples are recombined to approximate the full posterior [36; 43]. Our use of subhypergraphs is different in purpose: we do not recombine local simulations to approximate a global posterior. Instead, fixed-size subhypergraph sampling gives a controlled generative benchmark in which all methods are compared at matched node–hyperedge dimensions while preserving local higher-order incidence structure from the original large hypergraph.

For a hypergraph incidence matrix  $H \in \{0, 1\}^{n \times m}$ , rows correspond to nodes and columns correspond to hyperedges. Table 2 reports basic structural properties of the full benchmark hypergraphs before subhypergraph sampling. We include the number of nodes  $n$ , number of hyperedges  $m$ , average hyperedge size

$$\bar{d}_E = \frac{1}{m} \sum_{j=1}^m \sum_{i=1}^n H_{ij},$$

average node degree

$$\bar{d}_V = \frac{1}{n} \sum_{i=1}^n \sum_{j=1}^m H_{ij},$$

and incidence density

$$\rho = \frac{1}{nm} \sum_{i=1}^n \sum_{j=1}^m H_{ij} = \frac{\bar{d}_E}{n} = \frac{\bar{d}_V}{m}.$$

The feature and class columns are included only to identify the original benchmark datasets; these quantities are not used by the generative model.

**Cora.** Cora is used in its cocitation hypergraph form [45; 11]. Nodes correspond to papers, and hyperedges encode citation-induced contexts among papers. Thus,  $H_{ij} = 1$  indicates that paper  $i$  participates in citation context  $j$ . This dataset is sparse, with small average hyperedge size and low average node degree, making it a useful benchmark for testing whether a generator can reproduce academic incidence patterns without over-densifying the generated hypergraphs. We emphasise that this is the cocitation Cora dataset, not the coauthorship Cora dataset.

**CiteSeer.** CiteSeer is another cocitation-style academic hypergraph [45; 11]. Nodes are papers and hyperedges correspond to citation-induced groups. It has a similar semantic structure to Cora but differs in size, feature dimension, class structure, sparsity, and hyperedge incidence profile. It therefore tests whether performance on citation-derived hypergraphs is robust across related but distinct bibliographic datasets.

**DBLP.** DBLP is used as a coauthorship hypergraph [45; 11]. Nodes correspond to authors, and each hyperedge corresponds to the author set of a publication. Thus,  $H_{ij} = 1$  means that author  $i$  appears on publication  $j$ . This dataset differs from the cocitation benchmarks because hyperedges represent explicit group interactions rather than citation-derived contexts. It is a natural benchmark for evaluating whether a generator captures collaborative group-size distributions, repeated author participation, and overlap between author teams.

**House-Committees.** House-Committees is a congressional committee hypergraph [13]. Nodes correspond to members of the United States House of Representatives, and hyperedges correspond to committees. An incidence entry  $H_{ij} = 1$  indicates that representative  $i$  serves on committee  $j$ . Compared with the academic datasets, House-Committees is much denser and has substantially larger hyperedges. It therefore provides a useful stress test for models of group membership, because the generator must reproduce both large committee sizes and structured overlap between committees.

**Actor.** Actor is a heterogeneous benchmark derived from the actor-only induced subgraph of a larger film-director-actor-writer network [40]. In the version used here, nodes correspond to actors and hyperedges encode co-occurrence contexts derived from the benchmark construction. In incidence form,  $H_{ij} = 1$  records that actor  $i$  participates in context  $j$ . This dataset has a different semantic origin from citation, coauthorship, and committee data: hyperedges arise from media co-appearance. It is therefore useful for evaluating whether HEDGE captures incidence structure beyond academic and institutional domains.

**Twitch.** Twitch is a heterogeneous benchmark derived from social-network data on the Twitch streaming platform [27]. In the version used here, nodes correspond to users or accounts, while hyperedges encode shared Twitch-related contexts from the benchmark construction. In this paper, all attributes and labels are discarded and only the binary incidence relation is used. Twitch provides an online social-platform domain and tests whether HEDGE can capture sparse but non-academic incidence patterns with moderate hyperedge sizes.

**Use in the generative benchmark.** The original datasets are not used as independent samples from a population of hypergraphs. Instead, each real dataset is a single observed hypergraph. To obtain a controlled generative evaluation, we sample a bank of fixed-size subhypergraphs from the observed hypergraph, train on one subset, and compare generated samples against held-out subhypergraphs of the same size. This protocol controls the node and hyperedge dimensions of the incidence matrices, so the evaluation focuses on whether a method can reproduce incidence-space structure at a fixed scale.

## B.2 Evaluation metrics

We evaluate generated hypergraphs by comparing a batch of held-out *real* incidence matrices with a batch of *generated* incidence matrices. Let

$$\mathcal{H}_{\text{real}} = \{H_1^{(r)}, \dots, H_{N_r}^{(r)}\}, \quad \mathcal{H}_{\text{gen}} = \{H_1^{(g)}, \dots, H_{N_g}^{(g)}\},$$

where each incidence matrix has fixed size  $H \in \{0, 1\}^{n \times m}$ . For a hypergraph  $H$ , write

$$d_V(H) = H\mathbf{1}_m \in \mathbb{R}^n, \quad d_E(H) = H^\top \mathbf{1}_n \in \mathbb{R}^m,$$

for the node-degree and hyperedge-size vectors, respectively. Lower is better for all reported metrics.

In the main real-data comparison tables we report a compact set of *primary metrics* that target the structural properties most central to incidence-space hypergraph generation: density calibration, mean node degree, mean hyperedge size, distributional agreement for node degrees and hyperedge sizes, and higher-order overlap structure. These are defined below.

**Calibration-style summary gaps.** For a batch  $\mathcal{H}$ , define the mean incidence density, mean node degree, and mean hyperedge size by

$$\rho(\mathcal{H}) = \frac{1}{|\mathcal{H}|nm} \sum_{H \in \mathcal{H}} \sum_{i=1}^n \sum_{j=1}^m H_{ij},$$

$$\bar{k}(\mathcal{H}) = \frac{1}{|\mathcal{H}|n} \sum_{H \in \mathcal{H}} \sum_{i=1}^n d_V(H)_i, \quad \bar{e}(\mathcal{H}) = \frac{1}{|\mathcal{H}|m} \sum_{H \in \mathcal{H}} \sum_{j=1}^m d_E(H)_j.$$

We report the signed gaps

$$\Delta\rho = \rho(\mathcal{H}_{\text{gen}}) - \rho(\mathcal{H}_{\text{real}}), \quad \Delta k = \bar{k}(\mathcal{H}_{\text{gen}}) - \bar{k}(\mathcal{H}_{\text{real}}), \quad \Delta e = \bar{e}(\mathcal{H}_{\text{gen}}) - \bar{e}(\mathcal{H}_{\text{real}}).$$

These quantify whether the generator systematically over- or under-produces overall incidence density, average node participation, and average hyperedge size.

**Node-degree distribution metric.** Let

$$D_V(\mathcal{H}) = \{d_V(H)_i : H \in \mathcal{H}, i = 1, \dots, n\}$$

denote the pooled node-degree sample across the batch. We compare real and generated batches using the one-dimensional Wasserstein distance

$$W_1(k) := W_1(D_V(\mathcal{H}_{\text{real}}), D_V(\mathcal{H}_{\text{gen}})).$$

This measures whether the generator reproduces the full distribution of node participation counts, not only its mean.

**Hyperedge-size distribution metric.** Similarly, let

$$D_E(\mathcal{H}) = \{d_E(H)_j : H \in \mathcal{H}, j = 1, \dots, m\}$$

denote the pooled hyperedge-size sample. We report

$$W_1(e) := W_1(D_E(\mathcal{H}_{\text{real}}), D_E(\mathcal{H}_{\text{gen}})).$$

This measures whether the generator reproduces the distribution of group sizes, which is one of the most basic structural signatures of a hypergraph.

**Spectral Wasserstein distances.** For each hypergraph  $H$ , let  $L_V(H)$  be the node-side hypergraph Laplacian and  $L_E(H)$  the hyperedge-overlap Laplacian used by HEDGE. Writing their eigenvalues in nondecreasing order as

$$0 \leq \lambda_1^V(H) \leq \dots \leq \lambda_n^V(H), \quad 0 \leq \lambda_1^E(H) \leq \dots \leq \lambda_m^E(H),$$

we retain the first  $K$  eigenvalues from each side and pool them across the batch:

$$\Lambda_V^K(\mathcal{H}) = \{\lambda_i^V(H) : H \in \mathcal{H}, i = 1, \dots, \min(K, n)\},$$

$$\Lambda_E^K(\mathcal{H}) = \{\lambda_i^E(H) : H \in \mathcal{H}, i = 1, \dots, \min(K, m)\}.$$

The node spectral Wasserstein distance and edge spectral Wasserstein distance are

$$\text{Node spec. WD} = W_1(\Lambda_V^K(\mathcal{H}_{\text{real}}), \Lambda_V^K(\mathcal{H}_{\text{gen}})),$$

$$\text{Edge spec. WD} = W_1(\Lambda_E^K(\mathcal{H}_{\text{real}}), \Lambda_E^K(\mathcal{H}_{\text{gen}})).$$

The node-side spectrum probes global connectivity and diffusion geometry induced by node–hyperedge incidence, while the edge-side spectrum probes the geometry of hyperedge overlap. These metrics therefore assess whether generated samples match operator-level structure, not only degree, size, or overlap marginals.

**Overlap-tail mass.** To probe genuinely higher-order structure, we measure how often distinct hyperedges overlap in more than one node. For a hypergraph  $H$ , define the pairwise hyperedge-overlap matrix

$$O(H) = H^\top H,$$

and let

$$\mathcal{I}(H) = \{O_{jk}(H) : 1 \leq j < k \leq m\}$$

be the multiset of off-diagonal pairwise hyperedge intersections. We then define the overlap-tail mass above threshold 2 by

$$T_2(H) = \frac{1}{|\mathcal{I}(H)|} \sum_{z \in \mathcal{I}(H)} \mathbf{1}\{z \geq 2\}.$$

The reported batch-level tail-gap metric is

$$\text{Tail gap} = \left| \frac{1}{N_r} \sum_{a=1}^{N_r} T_2(H_a^{(r)}) - \frac{1}{N_g} \sum_{b=1}^{N_g} T_2(H_b^{(g)}) \right|.$$

This statistic is sensitive to repeated multi-node overlap between distinct hyperedges, and therefore helps distinguish generators that match only marginal degree/size behaviour from those that also reproduce higher-order shared membership structure.

**Intersection-distribution Wasserstein distance.** To compare the full distribution of pairwise hyperedge overlaps, not only its tail mass, we again use the multiset

$$\mathcal{I}(H) = \{(H^\top H)_{jk} : 1 \leq j < k \leq m\}.$$

Pooling these values across a batch gives

$$\mathcal{I}(\mathcal{H}) = \bigcup_{H \in \mathcal{H}} \mathcal{I}(H).$$

We then define the intersection Wasserstein distance by

$$\text{Intersection WD} := W_1(\mathcal{I}(\mathcal{H}_{\text{real}}), \mathcal{I}(\mathcal{H}_{\text{gen}})).$$

This metric is more stringent than Tail gap because it compares the full distribution of pairwise hyperedge intersections rather than only the mass in its upper tail.

**Feature MMD.** To compare broader structural signatures, we compute a feature vector  $\phi(H) \in \mathbb{R}^d$  for each hypergraph and then measure discrepancy between the real and generated feature samples using maximum mean discrepancy (MMD). In our experiments,  $\phi(H)$  consists of structural summaries derived from the incidence pattern, including marginal and overlap-sensitive quantities. Given feature sets

$$\Phi_{\text{real}} = \{\phi(H) : H \in \mathcal{H}_{\text{real}}\}, \quad \Phi_{\text{gen}} = \{\phi(H) : H \in \mathcal{H}_{\text{gen}}\},$$

the reported feature MMD is the empirical kernel MMD between these two samples:

$$\text{Feature MMD} = \text{MMD}(\Phi_{\text{real}}, \Phi_{\text{gen}}).$$

Lower values indicate closer agreement between real and generated hypergraphs in the chosen structural feature space.

### B.3 Ablation results

We use controlled simulated hypergraph distributions to isolate the modelling choices in HEDGE. The real-data experiments in Section 5 evaluate the final model against external baselines, whereas the simulations here are designed to answer a more specific question: whether the structured heat–OU forward process and the two-sided incidence operator improve generation quality relative to simpler variants under matched training and sampling budgets. All tables report mean  $\pm$  standard error across random seeds, and lower values are better for all reported metrics; metric definitions are given in Section B.2.

The simulated datasets cover four qualitatively different regimes. The CONFIGURATION regime emphasises heterogeneous degree and hyperedge-size marginals. The OVERLAPPING BLOCKS regime contains latent group structure with repeated higher-order overlap. The COMMITTEE regime is a denser group-membership setting with broad hyperedge sizes and structured overlap. The SPARSE TAIL OVERLAP regime is sparse overall but contains a controlled minority of hyperedge pairs with nontrivial intersections. Together these settings separate marginal calibration from the higher-order overlap and spectral structure that HEDGE is designed to model.

**Summary of the simulated ablations.** Table 1 gives the compact main-paper summary of the simulated ablation study, after first averaging each variant within synthetic dataset. The full HEDGE setting is consistently strongest or near-strongest on the structural metrics most directly aligned with the method’s objective: pairwise hyperedge-intersection distributions, overlap-tail mass, node- and edge-side spectra, and multivariate Feature MMD. The pure OU, node-only, and edge-only variants can be competitive on individual metrics, but they do not give the same overall balance across the structural suite of experiments. This supports the central modelling choice in HEDGE: the forward process should not be merely an unstructured Gaussian corruption, nor should it smooth only one side of the incidence matrix. The most reliable behaviour is obtained by combining structured heat with the OU terminal mechanism and by using both node-side and hyperedge-side geometry.

**Forward-process ablation.** Table 3 compares the full structured heat–OU model with a pure OU variant. The full model uses the proposed forward process: early-time noising is guided by the hypergraph heat operator, while late-time dynamics transition to the OU mechanism that yields a Gaussian base law. The PURE OU variant removes the hypergraph heat term and therefore tests whether generic OU corruption, together with the same learned reverse model, is sufficient.

The main pattern is that the heat–OU model is consistently stronger on the metrics most closely aligned with higher-order incidence structure. It improves Intersection WD on all four simulated regimes, with particularly clear gains on COMMITTEE and OVERLAPPING BLOCKS. It also improves Feature MMD on all four regimes and gives better node-side spectral agreement throughout. The edge-side spectral metric is also improved in three of four regimes, with the exception of CONFIGURATION, where the pure OU variant is competitive on edge-spectrum and degree-marginal quantities. This exception is informative rather than problematic: in the configuration-like setting, much of the data distribution is explained by first-order degree and size heterogeneity, so an unstructured OU perturbation can match some marginals well. However, once the evaluation focuses on overlap distributions, spectra, and multivariate structural features, the structured heat–OU process gives the better overall match.

The Tail gap metric is deliberately more local than Intersection WD: it measures only the mass of hyperedge pairs intersecting in at least two nodes. This makes it somewhat more variable across regimes. For example, pure OU has a smaller Tail gap on OVERLAPPING BLOCKS and SPARSE TAIL OVERLAP, while the full model is better on COMMITTEE and CONFIGURATION. We therefore interpret the forward-process ablation through the combined structural suite rather than through a single metric. On this combined view, the full heat–OU process is preferable because it improves the full intersection distribution, operator spectra, and feature-space discrepancy without requiring the degree and size sequences as inputs.

Dataset	Variant	Deg. WD	Size WD	Intersect. WD	Tail gap	Node spec. WD	Edge spec. WD	Feature MMD
Committee	Full heat OU	0.243 ± 0.033	0.305 ± 0.009	0.044 ± 0.005	0.013 ± 0.000	0.005 ± 0.001	0.002 ± 0.000	0.073 ± 0.031
	Pure OU	0.245 ± 0.074	0.310 ± 0.111	0.104 ± 0.057	0.028 ± 0.012	0.009 ± 0.002	0.004 ± 0.002	0.100 ± 0.027
Configuration	Full heat OU	0.267 ± 0.013	0.282 ± 0.010	0.025 ± 0.001	0.005 ± 0.000	0.022 ± 0.003	0.008 ± 0.000	0.069 ± 0.022
	Pure OU	0.203 ± 0.005	0.301 ± 0.015	0.032 ± 0.013	0.011 ± 0.005	0.035 ± 0.002	0.005 ± 0.001	0.089 ± 0.019
Overlapping blocks	Full heat OU	0.131 ± 0.024	0.168 ± 0.032	0.333 ± 0.013	0.021 ± 0.002	0.095 ± 0.003	0.124 ± 0.002	1.106 ± 0.110
	Pure OU	0.127 ± 0.018	0.177 ± 0.024	0.366 ± 0.003	0.005 ± 0.001	0.102 ± 0.001	0.129 ± 0.001	1.280 ± 0.027
Sparse tail overlap	Full heat OU	0.128 ± 0.019	0.164 ± 0.013	0.018 ± 0.002	0.007 ± 0.001	0.016 ± 0.006	0.012 ± 0.001	0.078 ± 0.020
	Pure OU	0.112 ± 0.017	0.213 ± 0.019	0.025 ± 0.004	0.004 ± 0.001	0.031 ± 0.004	0.018 ± 0.004	0.095 ± 0.030

Table 3: Simulated-data HEDGE forward process ablation. Values are mean ± standard error across seeds; lower is better.

**Two-sided incidence geometry.** Table 4 ablates the heat operator itself. The TWO-SIDED variant uses

$$\mathcal{A}_H(X) = L_V(H)X + XL_E(H),$$

where the first term smooths across nodes and the second smooths across overlapping hyperedges. The NODE ONLY variant removes the hyperedge-side overlap term, giving  $\mathcal{A}_H(X) = L_V(H)X$ . The EDGE ONLY variant removes the node-side term, giving  $\mathcal{A}_H(X) = XL_E(H)$ . The PURE OU row is included as an unstructured reference.

The two-sided operator is most clearly beneficial in regimes where higher-order overlap is central. On COMMITTEE, the two-sided model is best on Intersection WD, Tail gap, node-spectrum WD, edge-spectrum WD, and hyperedge-size WD, while remaining competitive on degree WD and Feature MMD. On OVERLAPPING BLOCKS, it is best on hyperedge-size WD, Intersection WD, node-spectrum WD, edge-spectrum WD, and Feature MMD. These two regimes are the closest simulated analogues of the structural phenomena targeted by HEDGE: co-membership, block overlap, and repeated shared participation. In these cases, using both node-side and hyperedge-side geometry gives the best overall structural fidelity.

The remaining regimes show a more nuanced pattern. On CONFIGURATION, simpler variants can match degree, size, and some overlap statistics more closely, which is expected because the data-generating mechanism is dominated by marginal degree and size constraints rather than rich overlap geometry. On SPARSE TAIL OVERLAP, the node-only and edge-only variants perform very well on some marginal and feature metrics, while the two-sided model remains competitive on the overlap and spectral quantities. This indicates that when overlap structure is deliberately sparse and localised, one side of the incidence geometry can sometimes be sufficient. The important point is that the two-sided operator is not merely a marginal-matching device: its advantage appears most clearly in the regimes where node participation and hyperedge overlap jointly determine the data distribution.

**Summary.** The ablations support the modelling assumptions behind HEDGE, but they also show that the result is not a trivial uniform sweep. Pure OU dynamics and one-sided operators can match some first-order marginals, especially in configuration-like or very sparse regimes. However, the proposed heat-OU formulation and two-sided operator give the best balance on the higher-order criteria that motivate the method: pairwise hyperedge-intersection distributions, nontrivial overlap mass, node- and edge-side spectra, and multivariate structural feature discrepancy. This is the desired outcome. HEDGE is not designed merely to reproduce degree and size distributions; it is designed to preserve incidence-space geometry while retaining a tractable Gaussian terminal law for reverse-time generation.

#### B.4 Real-data table of results

Table 5 reports the six primary real-data comparison metrics used throughout the paper. The signed quantities  $\Delta\rho$ ,  $\Delta e$ , and  $\Delta k$  measure calibration of global incidence density, mean hyperedge size, and mean node degree relative to held-out real subhypergraphs. The nonnegative discrepancy measures  $W_1(e)$  and  $W_1(k)$  evaluate whether the full distributions of hyperedge sizes and node degrees are reproduced, rather than merely their means. Lower is better for all metrics. As for Table 6, this is an extension of Table 2 from the main paper, but with the inclusion of uncertainties on each of the reported metrics.

Table 5 reports the calibration and marginal-distribution metrics used in the real-data benchmark, while Table 6 reports the higher-order metrics emphasised in the main paper. The overall pattern is clear. HCM-MCMC is typically the strongest baseline on calibration-style quantities ( $\Delta\rho$ ,  $\Delta e$ ,  $\Delta k$ ) and on hyperedge-size distribution matching  $W_1(e)$ , which is consistent with its strong null-model behaviour on marginal statistics. HEDGE, however, is the most consistently strong method on the metrics that directly probe higher-order incidence structure. In particular, it achieves the best

Dataset	Variant	Deg. WD	Size WD	Intersect. WD	Tail gap	Node spec. WD	Edge spec. WD	Feature MMD
Committee	Edge only	0.364 ± 0.067	0.435 ± 0.108	0.107 ± 0.046	0.024 ± 0.012	0.010 ± 0.002	0.003 ± 0.001	0.201 ± 0.053
	Node only	0.212 ± 0.052	0.351 ± 0.060	0.117 ± 0.022	0.036 ± 0.007	0.008 ± 0.002	0.005 ± 0.001	0.053 ± 0.017
	Pure OU	0.245 ± 0.074	0.310 ± 0.111	0.104 ± 0.057	0.028 ± 0.012	0.009 ± 0.002	0.004 ± 0.002	0.100 ± 0.027
	Two-sided	0.243 ± 0.033	0.305 ± 0.009	0.044 ± 0.005	0.013 ± 0.000	0.005 ± 0.001	0.002 ± 0.000	0.073 ± 0.031
Configuration	Edge only	0.173 ± 0.012	0.210 ± 0.008	0.024 ± 0.008	0.006 ± 0.002	0.016 ± 0.003	0.007 ± 0.001	0.029 ± 0.006
	Node only	0.166 ± 0.016	0.246 ± 0.011	0.031 ± 0.006	0.010 ± 0.003	0.025 ± 0.002	0.005 ± 0.001	0.053 ± 0.026
	Pure OU	0.149 ± 0.020	0.226 ± 0.023	0.023 ± 0.002	0.005 ± 0.002	0.026 ± 0.002	0.003 ± 0.000	0.044 ± 0.019
	Two-sided	0.194 ± 0.009	0.248 ± 0.016	0.043 ± 0.015	0.014 ± 0.005	0.018 ± 0.006	0.008 ± 0.003	0.028 ± 0.008
Overlapping blocks	Edge only	0.208 ± 0.034	0.237 ± 0.054	0.355 ± 0.005	0.018 ± 0.004	0.098 ± 0.001	0.128 ± 0.000	1.201 ± 0.076
	Node only	0.193 ± 0.061	0.209 ± 0.061	0.385 ± 0.013	0.022 ± 0.007	0.097 ± 0.000	0.127 ± 0.001	1.285 ± 0.046
	Pure OU	0.127 ± 0.018	0.177 ± 0.024	0.366 ± 0.003	0.005 ± 0.001	0.102 ± 0.001	0.129 ± 0.001	1.280 ± 0.027
	Two-sided	0.131 ± 0.024	0.168 ± 0.032	0.333 ± 0.013	0.021 ± 0.002	0.095 ± 0.003	0.124 ± 0.002	1.106 ± 0.110
Sparse tail overlap	Edge only	0.075 ± 0.004	0.144 ± 0.015	0.019 ± 0.002	0.007 ± 0.002	0.011 ± 0.007	0.012 ± 0.002	0.062 ± 0.029
	Node only	0.067 ± 0.011	0.143 ± 0.007	0.014 ± 0.002	0.007 ± 0.001	0.013 ± 0.003	0.009 ± 0.001	0.023 ± 0.007
	Pure OU	0.112 ± 0.017	0.213 ± 0.019	0.025 ± 0.004	0.004 ± 0.001	0.031 ± 0.004	0.018 ± 0.004	0.095 ± 0.030
	Two-sided	0.128 ± 0.019	0.164 ± 0.013	0.018 ± 0.002	0.007 ± 0.001	0.016 ± 0.006	0.012 ± 0.001	0.078 ± 0.020

Table 4: Simulated-data HEDGE two-sided geometry ablation. Values are mean ± standard error across seeds; lower is better.

Table 5: Real-data direct comparison across the six main datasets. Entries are mean ± standard deviation over independent seeds. Lower is better in all metrics. For each dataset and metric, best is shown in **bold** and second-best is in *italics*. H.-Comm. = House Committees.

Metric	Method	Cora	CiteSeer	Actor	H.-Comm.	DBLP	Twitch
$\Delta\rho$	HEDGE	<i>0.001 ± 0.000</i>	<b>0.000 ± 0.002</b>	<i>-0.000 ± 0.001</i>	<i>-0.005 ± 0.004</i>	<i>0.003 ± 0.002</i>	<i>0.000 ± 0.001</i>
	HCM-MCMC	<b>0.000 ± 0.001</b>	<i>0.002 ± 0.004</i>	<b>-0.001 ± 0.001</b>	<b>-0.007 ± 0.005</b>	<b>-0.000 ± 0.004</b>	<b>-0.001 ± 0.002</b>
	ER-HG	0.017 ± 0.001	0.016 ± 0.001	0.023 ± 0.002	0.012 ± 0.004	0.021 ± 0.002	0.022 ± 0.002
	HYGENE	0.053 ± 0.026	0.411 ± 0.201	0.783 ± 0.165	0.060 ± 0.079	0.563 ± 0.216	0.910 ± 0.004
$\Delta e$	HEDGE	<i>0.063 ± 0.023</i>	<b>0.009 ± 0.142</b>	<i>-0.022 ± 0.067</i>	<i>-0.328 ± 0.255</i>	<i>0.165 ± 0.099</i>	<i>0.001 ± 0.064</i>
	HCM-MCMC	<b>0.017 ± 0.039</b>	<i>0.116 ± 0.224</i>	<b>-0.040 ± 0.070</b>	<b>-0.432 ± 0.324</b>	<b>-0.030 ± 0.269</b>	<b>-0.059 ± 0.105</b>
	ER-HG	1.107 ± 0.045	1.034 ± 0.067	1.455 ± 0.124	0.740 ± 0.235	1.317 ± 0.101	1.379 ± 0.118
	HYGENE	3.398 ± 1.680	26.31 ± 12.86	50.14 ± 10.59	3.844 ± 5.069	36.01 ± 13.85	58.27 ± 0.28
$\Delta k$	HEDGE	<i>0.025 ± 0.009</i>	<b>0.004 ± 0.055</b>	<i>-0.005 ± 0.017</i>	<i>-0.082 ± 0.064</i>	<i>0.046 ± 0.028</i>	<i>0.000 ± 0.016</i>
	HCM-MCMC	<b>0.007 ± 0.015</b>	<i>0.045 ± 0.088</i>	<b>-0.010 ± 0.018</b>	<b>-0.108 ± 0.081</b>	<b>-0.008 ± 0.076</b>	<b>-0.015 ± 0.026</b>
	ER-HG	0.432 ± 0.018	0.404 ± 0.026	0.364 ± 0.031	0.185 ± 0.059	0.371 ± 0.028	0.345 ± 0.029
	HYGENE	1.327 ± 0.656	10.28 ± 5.02	12.53 ± 2.65	0.961 ± 1.267	10.13 ± 3.89	14.57 ± 0.07
$W_1(e)$	HEDGE	<i>0.127 ± 0.038</i>	<i>0.358 ± 0.111</i>	<b>0.192 ± 0.082</b>	<b>0.547 ± 0.178</b>	<i>0.722 ± 0.155</i>	<i>0.354 ± 0.125</i>
	HCM-MCMC	<b>0.083 ± 0.035</b>	<b>0.292 ± 0.229</b>	<i>0.325 ± 0.122</i>	<i>0.661 ± 0.275</i>	<b>0.441 ± 0.100</b>	<b>0.346 ± 0.024</b>
	ER-HG	1.117 ± 0.069	1.130 ± 0.068	1.592 ± 0.122	1.245 ± 0.282	1.552 ± 0.378	1.299 ± 0.068
	HYGENE	3.395 ± 1.693	26.56 ± 12.82	57.33 ± 0.67	4.896 ± 4.848	36.89 ± 25.39	58.14 ± 0.26
$W_1(k)$	HEDGE	<b>0.048 ± 0.014</b>	<b>0.105 ± 0.022</b>	<b>0.050 ± 0.023</b>	<i>0.133 ± 0.033</i>	<i>0.174 ± 0.024</i>	<i>0.091 ± 0.011</i>
	HCM-MCMC	<i>0.056 ± 0.003</i>	<i>0.143 ± 0.094</i>	<b>0.050 ± 0.026</b>	<b>0.098 ± 0.037</b>	<b>0.101 ± 0.081</b>	<b>0.054 ± 0.026</b>
	ER-HG	0.431 ± 0.028	0.441 ± 0.027	0.358 ± 0.086	0.270 ± 0.073	0.403 ± 0.094	0.313 ± 0.022
	HYGENE	2.644 ± 0.757	10.60 ± 4.92	14.38 ± 0.15	1.625 ± 1.021	10.94 ± 6.43	14.54 ± 0.07

result on all six datasets for Intersection WD and on most datasets for Overlap Tail Gap and Feature MMD. Thus, relative to HCM-MCMC, HEDGE trades a small amount of marginal advantage for a substantial gain in capturing overlap-sensitive and higher-order structure. ER-HG is uniformly weaker on most datasets, and HYGENE performs poorly throughout, often by a wide margin.

## B.5 Bipartite Representations for Real-data Examples

Figures 3–6 provide a qualitative view of representative held-out real subhypergraphs and matched generated samples through their *bipartite representation*. A hypergraph incidence matrix  $H \in \{0, 1\}^{n \times m}$  may be viewed equivalently as a two-mode graph with one node set corresponding to vertices and the other corresponding to hyperedges: a left-side node  $v_i$  and a right-side node  $e_j$  are connected if and only if  $H_{ij} = 1$ . Thus each line in the bipartite plot represents exactly one node–hyperedge incidence. The plots are therefore visually equivalent to the incidence-matrix view, but often easier to read in terms of participation patterns, degree heterogeneity, and overlap structure.

In each figure, rows correspond to three representative held-out test subhypergraphs chosen by incidence-count tier (low, median, and high), while the generated examples are matched to the corresponding real example by nearest incidence

Table 6: Higher-order real-data comparison with uncertainty. Entries are reported as mean  $\pm$  standard deviation across seeds. Lower is better for all metrics; best mean values are **bold** and second-best mean values are in *italics*. H.-Comm. = House Committees.

Metric	Method	Cora	CiteSeer	Actor	H.-Comm.	DBLP	Twitch
Overlap Tail Gap	HEDGE	<b>0.005 <math>\pm</math> 0.001</b>	0.012 $\pm$ 0.005	<b>0.004 <math>\pm</math> 0.002</b>	<b>0.034 <math>\pm</math> 0.016</b>	<b>0.011 <math>\pm</math> 0.011</b>	<b>0.008 <math>\pm</math> 0.001</b>
	HCM-MCMC	<i>0.006 <math>\pm</math> 0.001</i>	<i>0.012 <math>\pm</math> 0.008</i>	<i>0.008 <math>\pm</math> 0.003</i>	<i>0.035 <math>\pm</math> 0.011</i>	0.016 $\pm$ 0.006	<i>0.018 <math>\pm</math> 0.003</i>
	ER-HG	0.006 $\pm$ 0.004	<b>0.005 <math>\pm</math> 0.003</b>	0.032 $\pm$ 0.018	0.130 $\pm$ 0.029	<i>0.012 <math>\pm</math> 0.014</i>	0.023 $\pm$ 0.004
	HYGENE	0.618 $\pm$ 0.301	0.738 $\pm$ 0.171	0.992 $\pm$ 0.003	0.419 $\pm$ 0.133	0.977 $\pm$ 0.006	0.980 $\pm$ 0.003
Intersection WD	HEDGE	<b>0.017 <math>\pm</math> 0.004</b>	<b>0.050 <math>\pm</math> 0.018</b>	<b>0.041 <math>\pm</math> 0.020</b>	<b>0.223 <math>\pm</math> 0.062</b>	<b>0.080 <math>\pm</math> 0.022</b>	<b>0.075 <math>\pm</math> 0.010</b>
	HCM-MCMC	<i>0.026 <math>\pm</math> 0.006</i>	<i>0.081 <math>\pm</math> 0.014</i>	<i>0.058 <math>\pm</math> 0.014</i>	<i>0.320 <math>\pm</math> 0.032</i>	<i>0.081 <math>\pm</math> 0.021</i>	<i>0.113 <math>\pm</math> 0.026</i>
	ER-HG	0.167 $\pm$ 0.003	0.187 $\pm$ 0.007	0.319 $\pm$ 0.043	0.612 $\pm$ 0.083	0.295 $\pm$ 0.040	0.334 $\pm$ 0.027
	HYGENE	4.390 $\pm$ 2.197	21.647 $\pm$ 15.046	61.557 $\pm$ 0.598	3.249 $\pm$ 2.716	40.132 $\pm$ 26.092	62.615 $\pm$ 0.245
Feature MMD	HEDGE	<i>0.123 <math>\pm</math> 0.050</i>	<b>0.053 <math>\pm</math> 0.026</b>	<b>0.136 <math>\pm</math> 0.079</b>	<b>0.072 <math>\pm</math> 0.073</b>	<b>0.083 <math>\pm</math> 0.089</b>	<b>0.101 <math>\pm</math> 0.085</b>
	HCM-MCMC	<b>0.110 <math>\pm</math> 0.032</b>	<i>0.194 <math>\pm</math> 0.181</i>	<i>0.277 <math>\pm</math> 0.145</i>	<i>0.163 <math>\pm</math> 0.128</i>	<i>0.102 <math>\pm</math> 0.007</i>	<i>0.159 <math>\pm</math> 0.019</i>
	ER-HG	1.059 $\pm$ 0.091	1.082 $\pm$ 0.079	0.928 $\pm$ 0.151	0.699 $\pm$ 0.231	0.951 $\pm$ 0.017	0.932 $\pm$ 0.116
	HYGENE	0.524 $\pm$ 0.080	0.802 $\pm$ 0.125	1.008 $\pm$ 0.288	0.422 $\pm$ 0.215	0.999 $\pm$ 0.280	0.890 $\pm$ 0.066

count. This controls for overall size, so that the visual comparison focuses on *how* incidences are arranged rather than simply on *how many* incidences are present. In particular, these plots make it possible to see whether a method reproduces (i) the overall sparsity level, (ii) variation in node participation and hyperedge sizes, and (iii) repeated concentration of incidences that induces nontrivial overlap between hyperedges.

The broad qualitative pattern agrees with the quantitative results in Tables 5 and 6. HEDGE generally reproduces the overall incidence organisation of the held-out examples more faithfully than the weaker baselines: its samples usually have the right visual density and exhibit structured, non-uniform incidence patterns rather than diffuse or nearly collapsed occupancy. HCM-MCMC is often visually competitive, which is consistent with its strong performance on marginal degree- and size-based statistics. However, HEDGE more often preserves the richer overlap-sensitive organisation that is harder to capture from marginals alone. By contrast, ER-HG tends to produce overly homogeneous incidence patterns, while HYGENE frequently appears degenerate on these fixed-size real-data examples, with incidences spread in a way that is visually inconsistent with the held-out subhypergraphs.

These figures should therefore be read as qualitative support for the main empirical claim of the paper. They do not replace the numerical evaluation, but they help explain *why* the higher-order metrics favour HEDGE: the model is not merely matching coarse sparsity, but is more consistently reproducing the structured incidence organisation that gives rise to realistic hyperedge overlap.

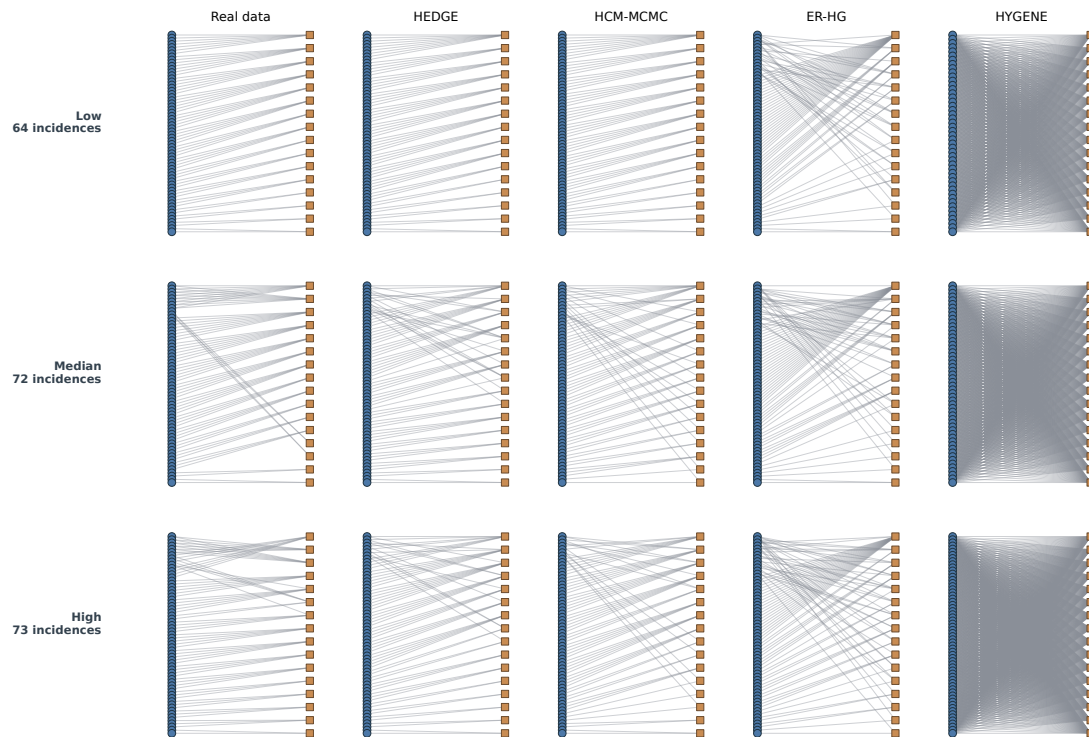


Figure 3: Actor dataset: Bipartite visualisation of held-out subhypergraph incidence matrices and matched generated samples. Each row shows a representative real test subhypergraph selected by incidence-count tier: low, median, or high, where an incidence is one node-hyperedge membership, shown as a line in the bipartite plot. Generated samples in the same row are size-matched to the real example by nearest incidence count.

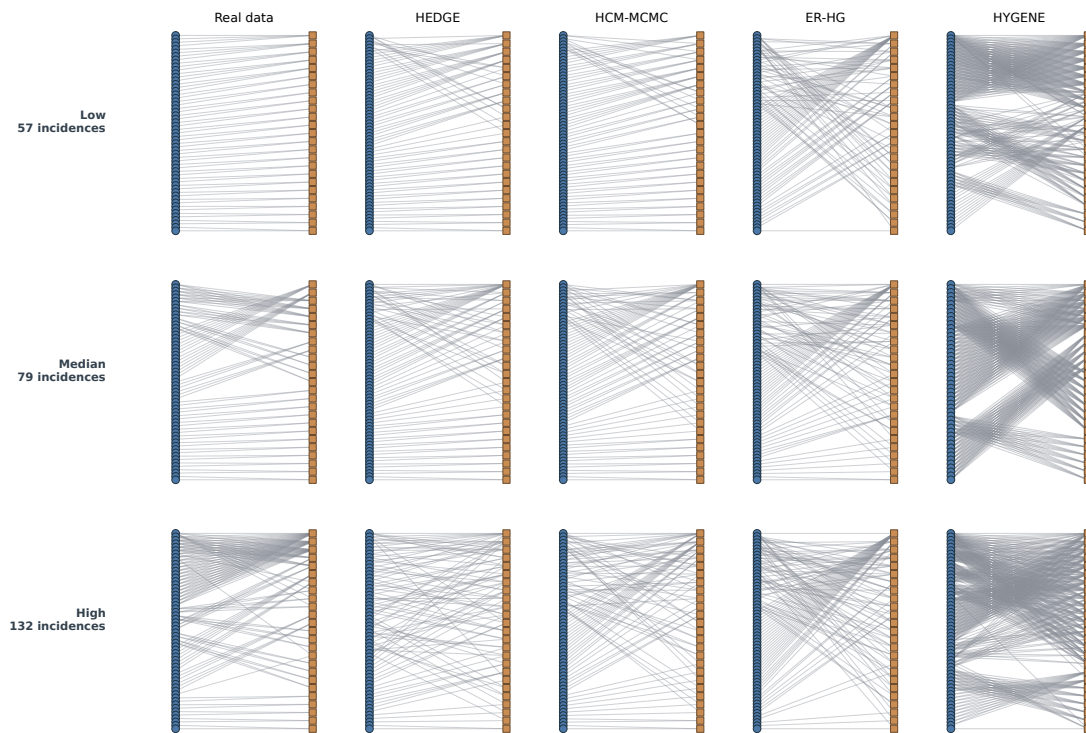


Figure 4: Citeseer dataset: Bipartite visualisation of held-out subhypergraph incidence matrices and matched generated samples. Each row shows a representative real test subhypergraph selected by incidence-count tier: low, median, or high, where an incidence is one node-hyperedge membership, shown as a line in the bipartite plot. Generated samples in the same row are size-matched to the real example by nearest incidence count.

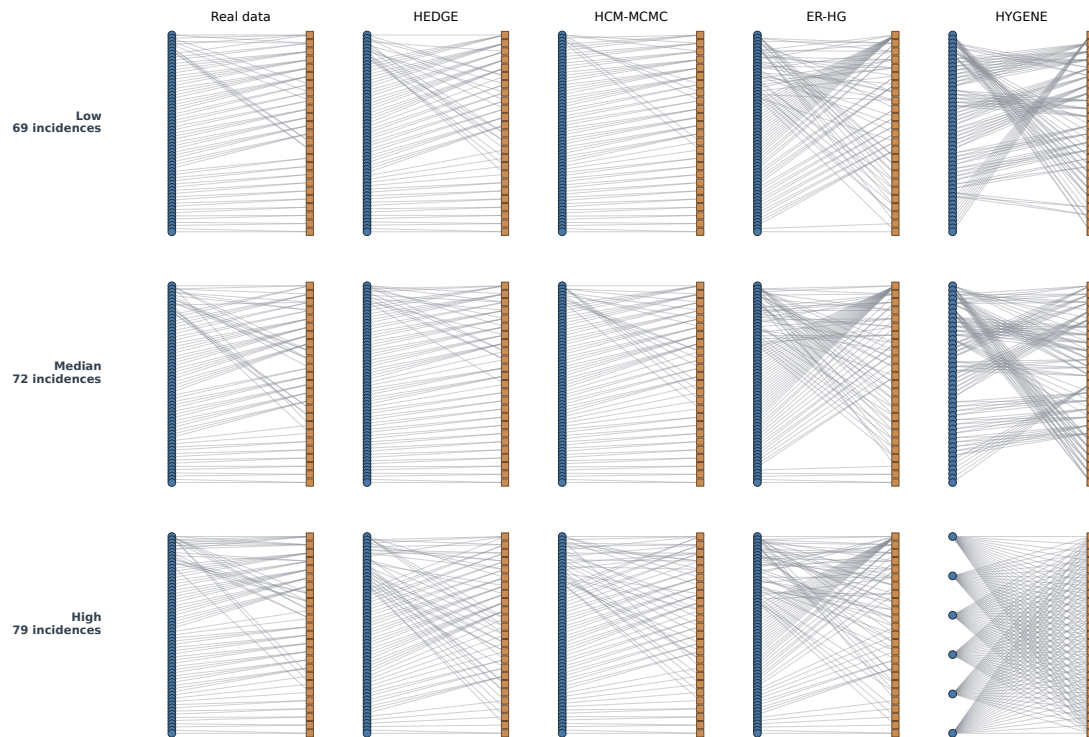


Figure 5: Cora dataset: Bipartite visualisation of held-out subhypergraph incidence matrices and matched generated samples. Each row shows a representative real test subhypergraph selected by incidence-count tier: low, median, or high, where an incidence is one node-hyperedge membership, shown as a line in the bipartite plot. Generated samples in the same row are size-matched to the real example by nearest incidence count.

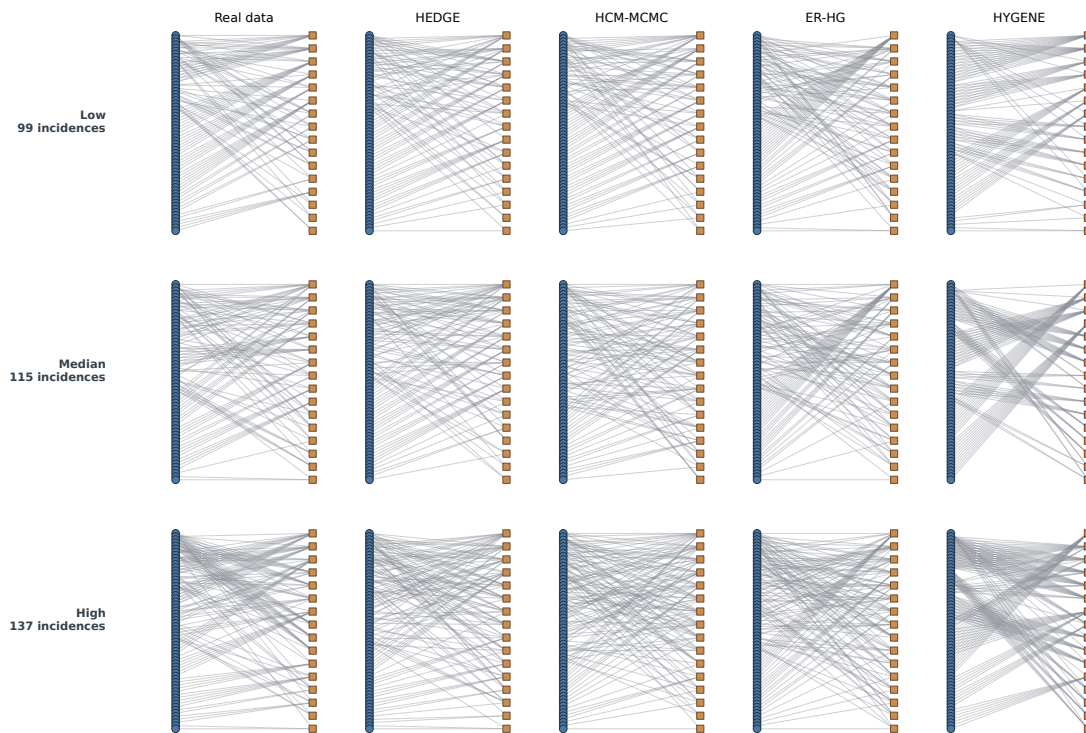


Figure 6: House committees dataset: Bipartite visualisation of held-out subhypergraph incidence matrices and matched generated samples. Each row shows a representative real test subhypergraph selected by incidence-count tier: low, median, or high, where an incidence is one node-hyperedge membership, shown as a line in the bipartite plot. Generated samples in the same row are size-matched to the real example by nearest incidence count.